Analysis and Stability Enhancement of an Inverter-Based Microgrid through the Design of an Advanced Droop Controller using a Modified PSO

Kinnari C. Matharani[1*] iD, Hitesh R. Jariwala[2] iD

[1,2] Electrical Engineering Department, Sardar Vallabhbhai National Institute of Technology, Surat, Gujarat, India
E-mail: kinbaheti@gmail.com

Abstract — Microgrids can operate in grid-tied mode and islanded mode with different load conditions. During the transition from one operating mode to another or varying load conditions, small disturbances may occur in the system, which can create transient oscillations due to the insufficient inertia of the distributed generating units (DG) of the microgrid. The droop control is mainly adapted to govern the working of the microgrid and maintain stability and power supply to the load. This paper presents an optimization-based control approach for the smooth operation of microgrids during the transition from one operating mode to another. The eigenvalue analysis and participation factors are used to find the control parameters for improving the power-sharing and stability of the microgrid. The modified PSO (MPSO) with adaptive weighted delayed velocity function (PSO-AWDV) is utilized to optimize the integral time square error (ITSE) of real and reactive power of the DGs in the microgrid. The eigenvalues analysis and time-domain simulation are presented to show the performance of the proposed approach for resistive and resistive-inductive load scenarios. The outcomes unveil that the optimized droop parameters improve the performance of DGs in microgrid by reducing overshoots in the range of 0.5% to 6% in real power, reactive power, output voltage, and currents of DGs as compared to parameters selected based on conventional approach. Moreover, the settling time for all the variables is reduced to 0.2 s with the proposed controller that enhances the steady state response of the system.

Keywords — Microgrid; Droop controller; Stability; Modified particle swarm optimization; Power sharing; Eigenvalue analysis.

1. INTRODUCTION

Distributed generating units (DGs) powered by renewable energy are the solution to the world's rising energy needs as well as its environmental and economic issues [1]. Integrating DGs, energy storage devices, and different loads is a well-established concept called "Microgrids" [2-5]. Microgrids are becoming popular because they provide clean energy, enable highly efficient combined heat and power generation (CHP) that reduces fuel consumption, line losses, and carbon footprints, increase the regional grid's reliability and resiliency, and offer ancillary services [6-8]. DGs in microgrids are coupled to the rest of the power system by power electronics-based controllers such as voltage source inverters (VSI) or current source inverters (CSI). The features of DGs are significantly more non-identical than the conventional AC generator. The control and operation of traditional power systems are well established, but in microgrids, the operation of generating sources is maintained by the control circuit of their interfacing inverters, and it is more challenging [9, 10]. The microgrid has two operational modes: grid-connected and islanded. While serving in connection with the grid, the reference

frequency and voltage of the microgrid are governed by the primary grid. Therefore, DGs in a microgrid function in PQ mode (Active and reactive power control) to supply desired powers to the load without relying on voltage and frequency [6, 11, 12]. When a microgrid operates in an islanded mode, apart from supplying power to the load, the voltage and frequency should also be sustained within limits by the DGs inverter control strategy, and therefore, VF mode (voltage and frequency control) is employed in an islanded mode [6, 12, 13]. VF mode can help distribute loads more effectively among different sources in microgrids with multiple generators by adjusting their power outputs based on frequency and voltage deviations.

When a microgrid changes the operating mode (grid-tied to islanded or vice versa) during the transition from one mode to another or during load change, small disturbances may occur in the system. The DGs in microgrids have low physical inertia; they respond to system disturbances much more quickly. These disturbances can cause transient oscillations in the system and hinder the microgrid's stability. [14]. The droop control technique can be enforced for microgrids in both operating modes and acquires the "plug and play" capability of DGs and loads.

For smooth operation of the microgrid during the changeover from one mode to another mode and during sudden load change, it is necessary to find the dominant control parameters from the stability point of view. Therefore, to enhance dampening in the transient state and achieve a fast steady-state response, the stability analysis is important.

The detailed state-space model of microgrids with different submodules is developed in [15, 16]. The reduced order state space models are developed in[17, 18]. In [19], the stability analysis of the converter regulates the ideal constant power load, and motor-driven dynamic power load is presented. The relation between stability and affecting factors is obtained in [20] and [21] by varying different control parameters, but no specific optimization scheme is used. In [22], all gains of the DGs controller are obtained using particle swarm optimization (PSO) without performing sensitivity analysis and, therefore, need further improvement.

In [23], the important control parameters are optimized using a genetic algorithm. The small signal stability analysis of the microgrid considering effect line dynamics is analyzed in [24] by optimizing droop parameters using a genetic algorithm. Multi-objective optimization using Lagrange multiplier is employed in [25] to improve power sharing and bus voltage regulation in islanded microgrid. The power quality is enhanced, and oscillations are dampened using the power differential term conventional droop [14].

The optimal power control of grid-connected VSI is discussed in [26] by optimizing all the PI controller gains for varying load conditions operation in PQ mode. In [27], the generalized droop control is suggested by modifying the control circuit of active power to overcome the shortfall of traditional droop and virtual synchronous generator control, but the design procedure of the developed controller is much more complex. Direct current vector control with conventional droop is suggested in [28] to amend the power quality and functionality of the microgrid. Dynamic droop scheme, considering the intermittent nature of generating source to overcome the inability of conventional droop to maintain an efficient operating point, is analyzed in [29].

The main contributions of the paper are as follows:
- This paper presents the detailed state-space model of the complete microgrid.
- The eigenvalue and sensitivity analysis are carried out to find parameters that are sensitive for the control and operation of the microgrid.

- The modified PSO (MPSO) with adaptive weighted delayed velocity function (AWDV) is applied to find the optimized value of control parameters.
- The time domain simulation is executed to analyze the adequacy of proposed technique for simple Resistive load and Resistive -Inductive load in different operating scenarios.

The paper is epitomized as follows. In Section 2, a model of a microgrid system with a droop-controlled inverter submodule, distribution line submodule, and load submodule is developed in state-space form. Section 3 presents the eigenvalue analysis and sensitivity analysis of the study system to obtain control parameters. In section 4, the control parameters are obtained using modified improved PSO with adaptive weighted delayed velocity function. Section 5 presents simulation results and eigenvalue analysis to show the efficacity of optimized parameters on system performance. Finally, the paper is concluded in section 6.

2. STATE-SPACE MODEL OF THE STUDY SYSTEM

The investigated system is represented in Fig. 1. It encompasses three parallel inverter-coupled DGs, coupling inductors and filters, distribution lines, and loads. The microgrid serves in grid-tied mode when the switch at PCC is closed. The DGs are outfitted with droop controllers to satisfy the power needs while regulating the system voltage and frequency.
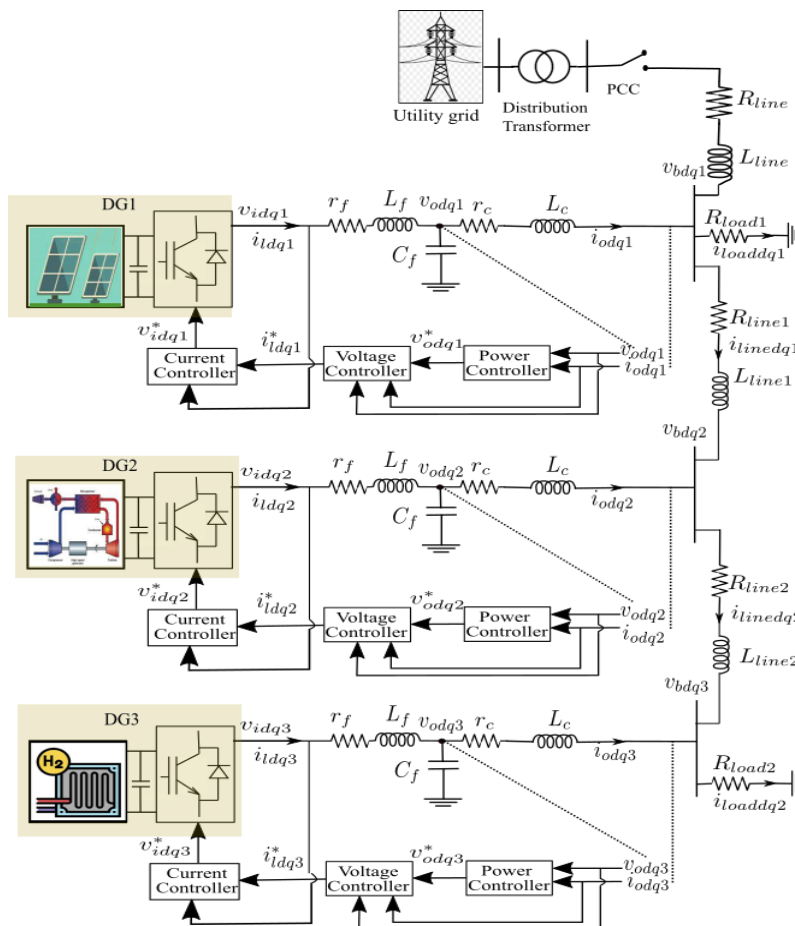

Fig. 1. The investigated system.

The droop gains of all the DGs are maintained the same to share the active power equally; however, because the distribution of reactive power depends on the local bus voltage to which DG is connected, the reactive power distribution among DGs may vary even if the reactive droop gain is the same.

The state-space model of a microgrid is divided into different submodules: Droop controlled inverter-coupled DGs, load, and network model. Each DG unit is represented by its own reference frame, the rotation frequency of which is determined by the power-sharing controller. The modelling of the network and load is formulated using a common reference frame. The individual submodules are modelled and integrated to extract the entire model of the microgrid. The detailed procedure for modelling the system is presented in the section below.

2.1.   Model of Droop-Controlled Inverter Coupled DGs

The DG units in a microgrid are interfaced with the network using three-phase voltage source inverters (VSI), LC filters, and coupling inductors. The switching operation of the inverter is omitted owing to the high frequency of VSI. The DC source side dynamics of the VSI are neglected, assuming that the source provides constant DC voltage. The controller of VSI comprises of an outer power-sharing controller, an inner voltage controller, and a current controller. The detailed model of each part is described in the subsection below.

2.1.1. Power Controller

Droop control is implemented in the power controller to generate reference voltage and frequency to share the powers across all DGs. The output voltage (v_{od}, v_{oq}) and output current (i_{od}, i_{oq}) of the DGs in dq reference frame are utilized to obtain instantaneous real power (P_{in}) and reactive power (Q_{in}) as defined in Eqs. (1) and (2).

$$P_{in} = v_{od}i_{od} + v_{oq}i_{oq} \tag{1}$$

$$Q_{in} = v_{oq}i_{od} - v_{od}i_{oq} \tag{2}$$

The average active and reactive power (P and Q) are derived from instantaneous power (P_{in} and Q_{in}) using a low pass filter (LPF), as shown in Fig. 2.
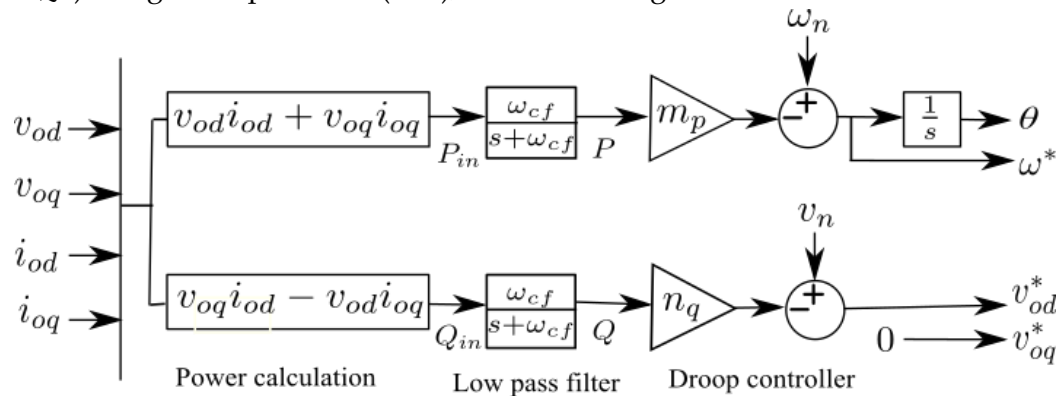

Fig. 2. The power Controller.

The extraction of powers is expressed as:

$$P = \frac{\omega_{cf}}{s + \omega_{cf}} P_{in}, \dot{P} = -P\omega_{cf} + \omega_{cf} P_{in} \tag{3}$$

$$Q = \frac{\omega_{cf}}{s + \omega_{c}f} Q_{in}, \dot{Q} = -Q\omega_{cf} + \omega_{cf} Q_{in}. \tag{4}$$

where ω_{cf} is the filter cut-off frequency of LPF.

The reference frequency (ω^*) and d-axis reference voltage (v_{od}^*) are obtained based on real droop gain (m_p) and reactive droop gain (n_q) from the natural frequency (ω_n) and nominal voltage $(v_{od,n})$. The q-axis voltage reference is set to zero.

$$\omega^* = \omega_n - m_p P \tag{5}$$

$$v_{od}^* = v_{od,n} - n_q Q \tag{6}$$

$$v_{oq}^* = 0 \tag{7}$$

The angle δ_j is defined for each DG inverter to transform from an individual reference frame to a common reference frame as,

$$\delta_j = \int (\omega_j - \omega_{com}) dt \tag{8}$$

where ω_j is the angular frequency of jth DG unit.

2.1.2. Voltage and Current Controllers

The voltage controller and current controller consist of the standard proportional and integral controller, as displayed in Fig. 3. They generate reference filter inductor currents (i_{ld}^*, i_{lq}^*) and reference inverter output voltages (v_{id}^*, v_{iq}^*) respectively.
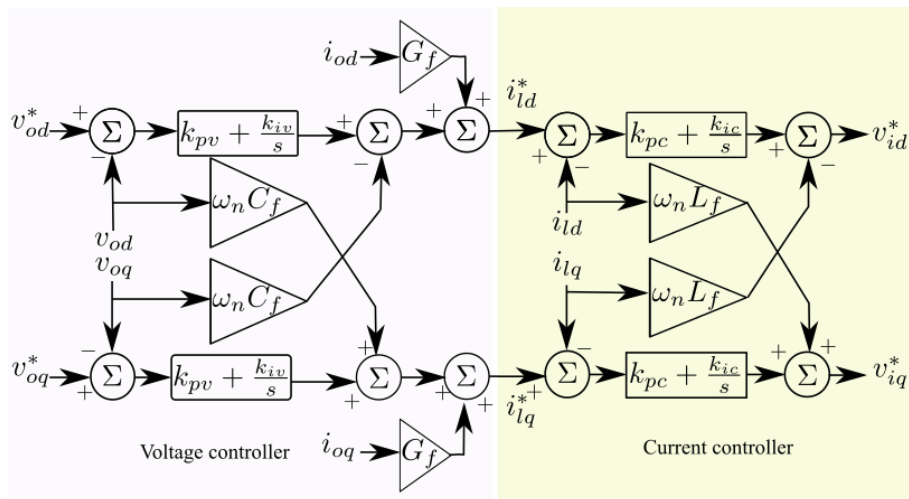

Fig. 3. Voltage and current controllers.

The modelling equations for the voltage controller are described in Eqs. (9) and (10), and algebraic equations in Eqs. (11) and (12).

$$\frac{d\phi_d}{dt} = v_{od}^* - v_{od} \tag{9}$$

$$\frac{d\phi_q}{dt} = v_{oq}^* - v_{oq} \tag{10}$$

where, ϕ_d and ϕ_q are state variables of the voltage controller.

$$i_{ld}^* = G_f i_{od} - \omega_n C_f v_{oq} + k_{pv}(v_{od}^* - v_{od}) + k_{iv}\phi_d \tag{11}$$

$$i_{lq}^* = G_f i_{oq} + \omega_n C_f v_{od} + k_{pv}(v_{oq}^* - v_{oq}) + k_{iv}\phi_q \tag{12}$$

where G_f is feed-forward gain, C_f is filter capacitance, k_{pv} and k_{iv} are proportional and the integral gain of the voltage controller, accordingly.

The modeling equations for the current controller are described in Eqs. (13) and (14), and algebraic equations in Eqs. (15) and (16).

$$\frac{d\gamma_d}{dt} = i_{ld}^* - i_{ld} \tag{13}$$

$$\frac{d\gamma_q}{dt} = i_{lq}^* - i_{lq} \tag{14}$$

where, γ_d and γ_q are state variables of the current controller.

$$v_{id}^* = -\omega_n L_f i_{lq} + k_{pc}(i_{ld}^* - i_{ld}) + k_{ic}\gamma_d \tag{15}$$

$$v_{iq}^* = \omega_n L_f i_{ld} + k_{pc}(i_{lq}^* - i_{lq}) + k_{ic}\gamma_q \tag{16}$$

where, L_f is filter capacitance, k_{pc} and k_{ic} are proportional and integral gains of the current controller, respectively.

2.1.3. LC Filter and Coupling Inductor Model

LC filter with coupling inductor forms an LCL filter that provides higher attenuation to harmonics and improved performance with a low value of inductive and capacitive elements (*L* and *C*). The inverter's output voltages (v_{id} and v_{iq}) are considered to be the same as the reference voltages (v_{id}^* and v_{iq}^*) produced by the current controller.

The state equations for LCL filter inductor currents, output currents, and output voltages are presented by,

$$\frac{di_{ld}}{dt} = \omega i_{lq} + \frac{1}{L_f}(v_{id} - v_{od} - r_f i_{ld}) \tag{17}$$

$$\frac{di_{lq}}{dt} = -\omega i_{ld} + \frac{1}{L_f}(v_{iq} - v_{oq} - r_f i_{lq}) \tag{18}$$

$$\frac{di_{od}}{dt} = \omega i_{oq} + \frac{1}{L_c}(v_{od} - v_{bd} - r_c i_{od}) \tag{19}$$

$$\frac{di_{oq}}{dt} = -\omega i_{od} + \frac{1}{L_c}(v_{oq} - v_{bq} - r_c i_{oq}) \tag{20}$$

$$\frac{dv_{od}}{dt} = \omega v_{oq} + \frac{1}{C_f}(i_{ld} - i_{od}) \tag{21}$$

$$\frac{dv_{oq}}{dt} = -\omega v_{od} + \frac{1}{C_f}(i_{lq} - i_{oq}) \tag{22}$$

where, L_f is the coupling inductor, r_c and r_f are the internal resistance of the coupling inductor and filter inductor, respectively.

2.1.4. Model of an Individual DG

The comprehensive model of each VSI-coupled DG is formed by using Eqs. (1) to (22). Each DG in a microgrid is modeled using an individual reference frame. The frequency of DG1 is considered as the base frequency, and all other DG variables are transformed.

The transformation technique defined in Eq. (23) is used to translate all the other DGs to this common reference frame,

$$
\left[f_{DQ} \right] = \begin{bmatrix} \cos\left(\delta_j\right) & -\sin\left(\delta_j\right) \\ \sin\left(\delta_j\right) & \cos\left(\delta_j\right) \end{bmatrix} \left[f_{dq} \right].
\tag{23}
$$

The complete model of an individual VSI-coupled DG is presented as,

$$
\left[\Delta \dot{x}_{dgi} \right] = A_{dgi} \left[\Delta x_{dgi} \right] + B_{dgi} \left[\Delta v_{bDQi} \right] + B_{i\omega com} \left[\Delta \omega_{com} \right]
\tag{24}
$$

$$
\begin{bmatrix} \Delta \omega_{dgi} \\ \Delta i_{odgi} \end{bmatrix} = \begin{bmatrix} C_{dg\omega i} \\ C_{dgci} \end{bmatrix} \left[\Delta x_{dgi} \right]
\tag{25}
$$

$$
\left[\Delta x_{dgi} \right] = \begin{bmatrix} \Delta \delta_i & \Delta P_i & \Delta Q_i & \Delta \phi_{dqi} & \Delta \gamma_{dqi} & \Delta i_{ldqi} & \Delta v_{odqi} & \Delta i_{odqi} \end{bmatrix}.
\tag{26}
$$

In Eqs. (24) to (26) Δx_{dgi} represents the state vector of ith DG unit. A_{dgi} is the state matrix, B_{dgi} input matrix corresponding to bus voltages (Δv_{bDQi}), $B_{i\omega com}$ is input matrix corresponding to $\Delta \omega_{com}$. The $\Delta \omega_{dgi}$ is output frequency and Δi_{odgi} is the output currents of ith DG unit in dq reference frame. $C_{dg\omega i}$ and C_{dgci} are output matrices corresponding to frequency and current. The detailed matrices are defined in the Appendix.

2.1.5. Model of all VSI-coupled DGs

Many VSI-coupled DGs work in parallel to each other in microgrids. The mathematical model of s parallel connected DGs can be presented as,

$$
\left[\Delta \dot{x}_{DG} \right] = A_{DG} \left[\Delta x_{DG} \right] + B_{DG} \left[\Delta v_{bDQ} \right]
\tag{27}
$$

$$
\left[\Delta i_{oDQ} \right] = C_{DGc} \left[\Delta x_{DG} \right]
\tag{28}
$$

$$
\left[\Delta x_{DG} \right] = \begin{bmatrix} \Delta x_{dg1} & \Delta x_{dg2} & \Delta x_{dg3} ..... \Delta x_{dgs} \end{bmatrix}.
\tag{29}
$$

In Eqs. (27) to (29) Δx_{DG} represents the state vector of all the parallel connected DGs. A_{DG} is the state matrix, B_{DG} input matrix corresponds to bus voltages (Δv_{bDQ}) and C_{DGc} is the output matrix. The matrices are defined in the Appendix.

2.2. Modelling of Network and Passive Load

The network, i.e., the distribution line that interconnects DGs and load, is modeled by an *RL* circuit (with R_{linei} and L_{linei} as parameters of the ith line connected between j^{th} and k^{th} node),

$$
\frac{di_{lineDi}}{dt} = \frac{-R_{linei}}{L_{linei}} i_{lineDi} + \omega i_{lineQi} + \frac{1}{L_{linei}} v_{bDj} - \frac{1}{L_{linei}} v_{bDk}
\tag{30}
$$

$$
\frac{di_{lineQi}}{dt} = \frac{-R_{linei}}{L_{linei}} i_{lineQi} - \omega i_{lineQi} + \frac{1}{L_{linei}} v_{bQj} - \frac{1}{L_{linei}} v_{bQk}.
$$

For a distribution network with n lines, the above equations can be defined as,

$$
\left[\Delta \dot{i}_{lineDQ} \right] = A_{LINE} \left[\Delta i_{lineDQ} \right] + B_{1LINE} \left[\Delta v_{bDQ} \right] + B_{2LINE} \Delta \omega
\tag{31}
$$

Where:

$$\left[\Delta i_{lineDQ}\right] = \left[\Delta i_{lineDQ1} \quad \Delta i_{lineDQ2} \quad \dots \quad \dots \quad \Delta i_{lineDQn}\right]^T \tag{32}$$

$$\left[\Delta v_{bDQ}\right] = \left[\Delta v_{bDQ1} \quad \Delta v_{bDQ2} \quad \dots \quad \dots \quad \Delta v_{bDQm}\right]^T \tag{33}$$

$$\Delta\omega = \Delta\omega_{com} \tag{34}$$

The passive load (R_{loadi}, L_{loadi}) connected at the ith node can be presented as,

$$\frac{di_{loadDi}}{dt} = \frac{-R_{loadi}}{L_{loadi}} i_{loadDi} + \omega i_{loadQi} + \frac{1}{L_{loadi}} v_{bDi} \tag{35}$$

$$\frac{di_{loadQi}}{dt} = \frac{-R_{loadi}}{L_{loadi}} i_{loadQi} - \omega i_{loadDi} + \frac{1}{L_{loadi}} v_{bQi} \tag{36}$$

For p number of loads connected in the system, the generalized equation can be defined as,

$$\left[\Delta \dot{i}_{loadDQ}\right] = A_{LOAD}\left[\Delta i_{loadDQ}\right] + B_{1LOAD}\left[\Delta v_{bDQ}\right] + B_{2LOAD}\Delta\omega \tag{37}$$

In Eq. (37),

$$\left[\Delta i_{loadDQ}\right] = \left[\Delta i_{loadDQ1} \quad \Delta i_{loadDQ2} \quad \dots \quad \dots \quad \Delta i_{loadDQp}\right]^T \tag{38}$$

2.3. Complete Microgrid Model

The local bus voltages v_{bDQi} are derived by introducing a large virtual shunt resistor at each local bus node. At each node, the voltage is calculated considering the incoming current as positive and the outgoing current as negative.

The node voltages at each local bus are defined as,

$$v_{bDi} = r_{VN}\left(i_{oDi} - i_{loadDi} + i_{lineDi}\right) \tag{39}$$

$$v_{bQi} = r_{VN}\left(i_{oQi} - i_{loadQi} + i_{lineQi}\right) \tag{40}$$

where r_{VN} is the virtual resistance connected between the local bus and the ground.

The node bus voltages for the system with m buses can be defined as,

$$\left[\Delta v_{bDQ}\right] = R_{VN}\left(M_{DG}\left[\Delta i_{oDQ}\right] + M_{LINE}\left[\Delta i_{lineDQ}\right] + M_{LOAD}\left[\Delta i_{loadDQ}\right]\right) \tag{41}$$

In Eq. (41) R_{VN} is a diagonal matrix of r_{VN} of size $2m \times 2m$. The connection matrix M_{DG} maps the DG connection on the network node. If j^{th} DG is connected to i^{th} the node, the element $M(i, j)$ will be, and all other elements in that row will be 0. The line mapping matrix M_{LINE} of size $2m \times 2n$ maps the distribution line connection to the local bus. If the line is connected between j^{th} and k^{th} node, based on the current direction, elements are assigned +1 (for current entering the node) and -1 (for current leaving the node). The load connection matrix M_{LOAD} of size $2m \times 2p$ maps the load connection to the node with -1.

The integrated mathematical model of the microgrid is provided below,

$$\begin{bmatrix} \Delta \dot{x}_{DG} \\ \Delta i_{lineDQ} \\ \Delta i_{loadDQ} \end{bmatrix} = A_{mg} \begin{bmatrix} \Delta x_{DG} \\ \Delta i_{lineDQ} \\ \Delta i_{loadDQ} \end{bmatrix}. \tag{42}$$

3.   EIGENVALUE AND SENSITIVITY ANALYSES.

The state-space model of the entire study system is developed as particularized in section 2. Fig. 4. represents the eigenvalue plot of the study system. The entire eigenvalue plot is categorized into three different groups. Group 1 contains low-frequency dominant eigenvalues. The participation factor calculated for these dominant modes is shown in Table 1. It can be concluded from the sensitivity analysis that the eigenvalue in group 1 is influenced by the state variables of the power controller of DGs. The droop controller gains decide the sharing of the power in the power controller as described in section 2.1.1. The plot of two dominant low-frequency complex eigenvalues for variation in m_p and n_q is displayed in Fig. 5. and Fig. 6. correspondingly.
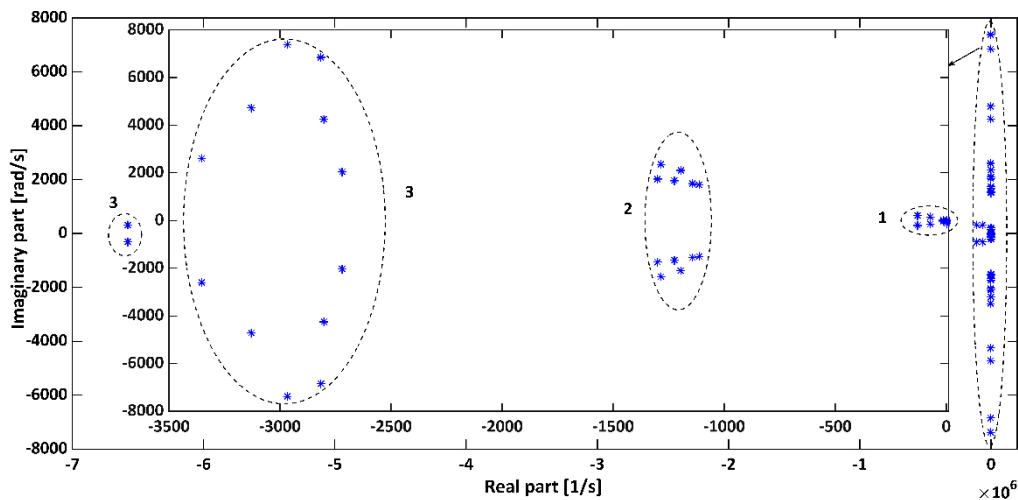

Fig. 4. Eigenvalue plot of the investigated system.

Table 1. Sensitivity analysis of low-frequency modes

| Sensitivity of mode 1 | | Sensitivity of mode 2 | |
State	Participation	State	Participation
P_1	0.45	P_1	0.11
Q_1	0.05	Q_1	0.05
P_2	0.15	P_3	0.4
Q_2	0.02	Q_3	0.03
δ_2	0.56	δ_3	0.57

Fig. 5 and Fig. 6 show that with an increase in the value of droop gains, the dominant modes shift towards the left side to the root-locus plane. The microgrid becomes marginally stable for the critical values of m_p (1.84×10^{-4}) and n_q (4.8×10^{-3}). Therefore, the droop gains m_p and n_q are selected as optimization control parameters. The optimization domain is selected based on the critical value of droop gain.

4.   OPTIMIZATION OF DROOP CONTROLLER PARAMETERS USING MPSO

PSO is a population-driven heuristic optimization method motivated by bird flocking, fish schooling, etc. It is a faster and more efficient algorithm than other optimization algorithms. It is best suited for solving continuous, discrete, nonlinear, and non-convex optimization problems [30, 31]. The conventional PSO has the problem of local trapping and premature

convergence. Many modifications have been suggested in the original PSO in literature, like grey PSO [32], ladder PSO [33], and dynamic PSO [34].
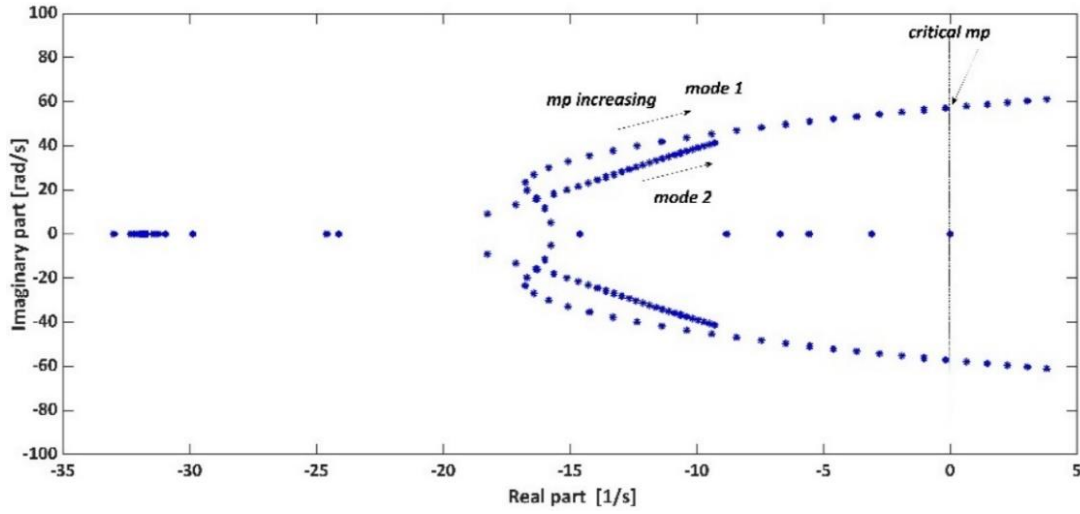

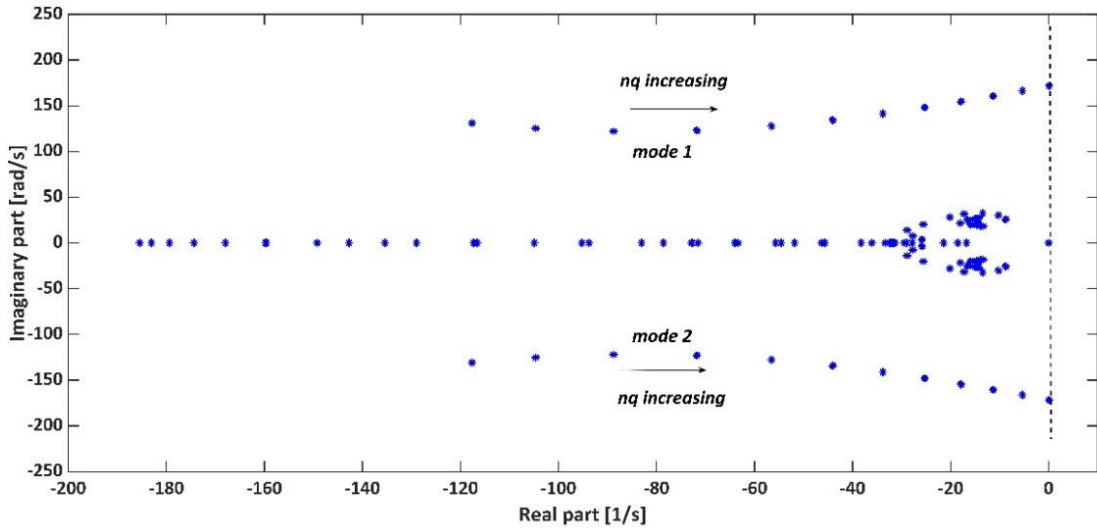Fig. 5. Low-frequency dominant eigenvalues for $1.57\text{e-}5 \leq m_p \leq 3.14\text{e-}4$.

Fig. 6. Low-frequency dominant eigenvalues for $3.17\text{e-}4 \leq n_q \leq 4.8\text{e-}3$.

This paper uses MPSO with AWDV function developed in [35] to obtain the optimized control parameters. The MPSO-AWDV is created by updating the velocity by using the delayed velocity function as an additional term.

It is almost similar to conventional PSO with one added term in the velocity equation to overcome the original PSO's shortfalls like premature convergence and local trapping. The adaptive weight is assigned to the velocity term and is calculated for each iteration using objective function values and other predefined constant parameters.

The microgrid can operate in grid-tied and autonomous modes; hence, an objective function is selected to ensure the optimized parameters give smoother operation in all operating modes. The integral time squared error (ITSE) of real and reactive power is chosen as an optimization function with real and reactive power as control variables. The objective function is defined in Eq. (43):

$$\min f = \sum_{i=1}^{n} \left\{ \int_{t_m=t_0^i}^{t_f^i} (t_m - t_0^i) \left[\left(P(t_m) - \left(P_{ref}\left(t_m\right) \right) \right)^2 + \left(Q(t_m) - \left(Q_{ref}\left(t_m\right) \right) \right)^2 \right] dt \right\}. \tag{43}$$

where n is the number of working modes for microgrid; t_m time at m^{th} instant. t_o^i and t_o^f are an initial and final time of operation in i^{th} mode. $P(t_m)$ and $Q(t_m)$ represents active and reactive power at instant t_m. $P_{ref}(t_m)$ and $Q_{ref}(t_m)$ represents the reference values of active and reactive power correspondingly. The optimization domain of droop controller gains is decided based on the critical value of root locus plots.

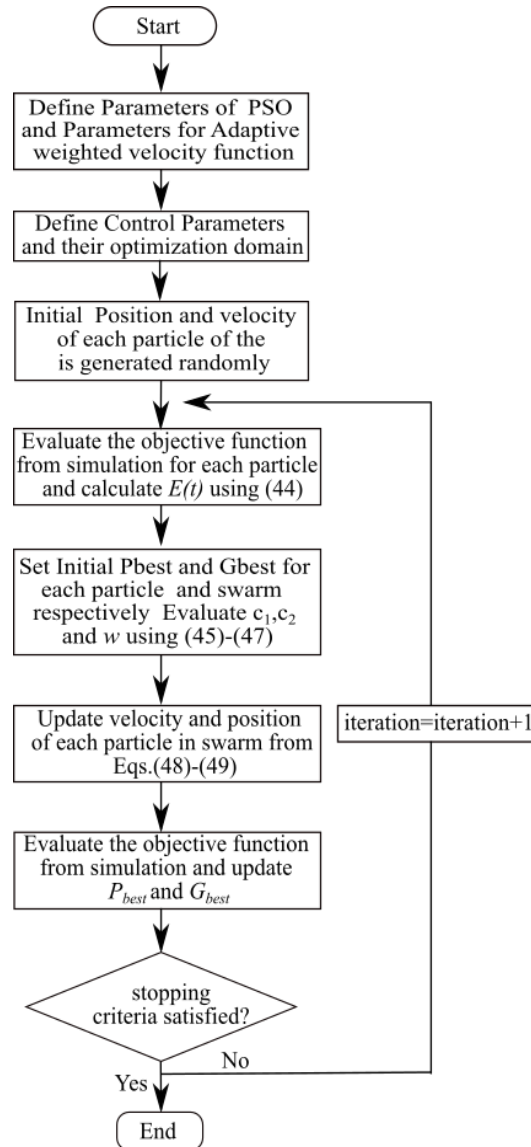The flow chart of MPSO is displayed in Fig. 7.

Fig. 7. Flowchart of MPSO.

The steps for the MPSO algorithm can be condensed as below.

Step 1: Read parameters of PSO, lower and upper boundaries of each control variable. Define parameters for calculation of adaptive weight for delayed velocity function (a, b, c_{1s}, c_{1f}, c_{2s}, c_{2f}).

Step 2: Randomly assign the initial position and velocity to all the particles in a population. The objective function is obtained from time domain simulation.

Step 3: The evolutionary state $E(t)$ is calculated for a given iteration from Eq. (44). The evolutionary state represents the weighted difference in objective function value. where max.

obj and min. obj is the maximal value and minimal value of the objective function correspondingly.

$$E(t) = \frac{|\max .obj(t)| - |\min .obj(t)|}{|\max .obj(t)|} \tag{44}$$

Step 4: The constant value of the acceleration factor in range (0,1) is generally selected for PSO. In modified PSO acceleration factors are updated using Eqs. (45) and (46) at each cycle.

$$C_{a1} = \left(c_{1s} - c_{1f}\right) \times \frac{\max .cycle - t}{\max .cycle} + c_{1f}, \tag{45}$$

$$C_{a2} = \left(c_{2s} - c_{2f}\right) \times \frac{\max .cycle - t}{\max .cycle} + c_{2f}, \tag{46}$$

Here c_{1s} and c_{1f} are the starting and final values of acceleration factor C_{a1}; c_{2s} and c_{2f} are the starting and final values of acceleration factor C_{a2}, maximal number of iterations is denoted by *max. cycle*, and t indicates the current iteration number.

Step 5: The nonlinear inertia weight is calculated from Eq. (47) by employing exponentially decreasing function. Inertia weight controls the velocity and delayed velocity of the particle at each iteration using:

$$w = 1 - \frac{a}{1 + e^{b*E(t)}} . \tag{47}$$

where a and b are parameters selected based on required search performance.

Step 6: The particle's velocity is calculated using Eqs. (48) and (49).

$$v_i(t+1) = wv_i(t) + (1-w)v_i(t-1) + C_{a1}r_1(P_{best}(t) - x_i(t)) + C_{a2}r_2(G_{best}(t) - x_i(t)) \tag{48}$$

The updated particle position is given by:

$$x_i(t+1) = x_i(t) + v_i(t+1) \tag{49}$$

where i is the particle count, v_i is the velocity of the ith particle, w and $(1-w)$ is the inertia weight of the velocity $v_i(t)$ and adjourned velocity $v_i(t-1)$, respectively,. x_i is the position of ith particle and P_{best} and G_{best} are the personal and global best of particle, respectively.

Step 7: The updated position and velocity of particles is used to find the new value of the objective function from time domain simulation.

Step 8: The P_{best} and G_{best} is updated by comparing recent P_{best} and G_{best} with previous values. If the recent value of the objective function for a particle is lesser than the previous best, the recent value is assigned as P_{best}.

Step 9: If maximum iterations is achieved or the error is within tolerance, then go to the next step; otherwise, repeat from Step 3.

Step 10: The particle position that generates the latest G_{best} is the optimum value of the control variables. PSO-AWDV is implemented considering 30 particles, and the maximum count of iterations is 50. Fig. 8. displays the convergence curve of an objective function for 50 iterations. The optimized real and reactive power droop gain value is 9×10^{-5} and 2×10^{-3}, respectively.

The droop controller gain value ensures a smooth changeover between different operation regimes and enhances microgrid power-sharing and stability grid. The aptness of

the designed droop controller is assessed in the next section, showing the eigenvalue and time-domain analysis of the study system in different operating modes.
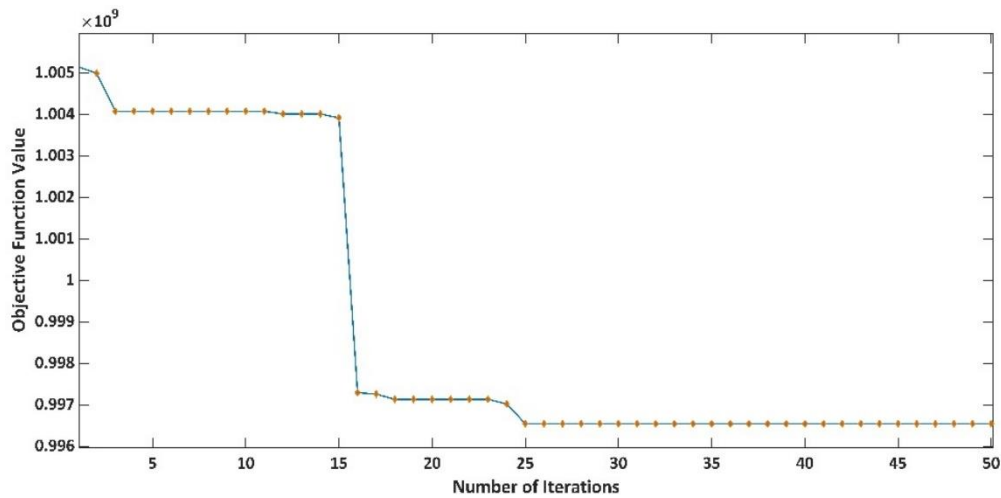

Fig. 8. Convergence curve of an objective function for 50 iterations.

5.   RESULTS AND DISCUSSION

To investigate the efficaciousness of the designed control strategy, time-domain simulation is performed for different working conditions for two cases: (i) with Resistive load only (ii) with Resistive-inductive load. The microgrid operates in (a) Grid-tied mode from t=0 s to t=0.8 s, (b) at t=0.8 s to t=1.8 s in islanded mode with initial load, and (c) at t=1.8 s to t=3 s the step reduction of load. The simulation results are evaluated with droop controller parameters selected based on the conventional approach and optimized droop gains obtained by MPSO.

The dominant low-frequency eigenvalue plot of the study system is presented in Fig. 9. It shows that the eigenvalues shift towards the right side of the root locus plane with optimized droop controller parameters and hence ameliorate the stability of the system.
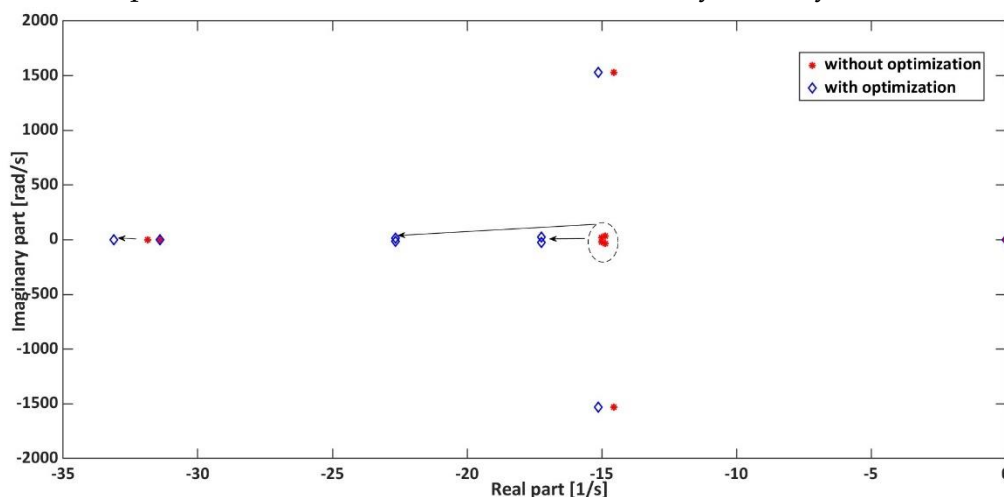

Fig. 9. Eigenvalue plot of dominant low-frequency modes.

Case 1: Considering only Resistive (R) load.

The microgrid initially operates in grid-connected mode with a resistive load. At t = 0.8 s, the grid is disconnected, and the microgrid operates in islanded mode. In this mode, the microgrid operates in droop control mode. The total load power is supplied by the three DGs, and the frequency and voltage of the microgrid are controlled by the droop controller. At

t = 0.8 s, the step reduction of load (3.88 kW) is applied, which is 30% of the total load, to see the effect of droop parameters on the performance of the microgrid. The time-domain simulation results for case 1 are discussed as follows:

Fig. 10 and Fig. 11 depict the system's real power and reactive power responses during transition and operation in different modes correspondingly. From Fig. 10, it can be observed that overshoot is reduced by 1.65%, 2.52%, and 0.08% in islanded mode, and undershoot is reduced by 1.2%, 0.9%, and 0.5% in load reduction mode with optimized parameters as compared to droop parameters obtained using the conventional approach for DG1, DG2, and DG3 respectively.
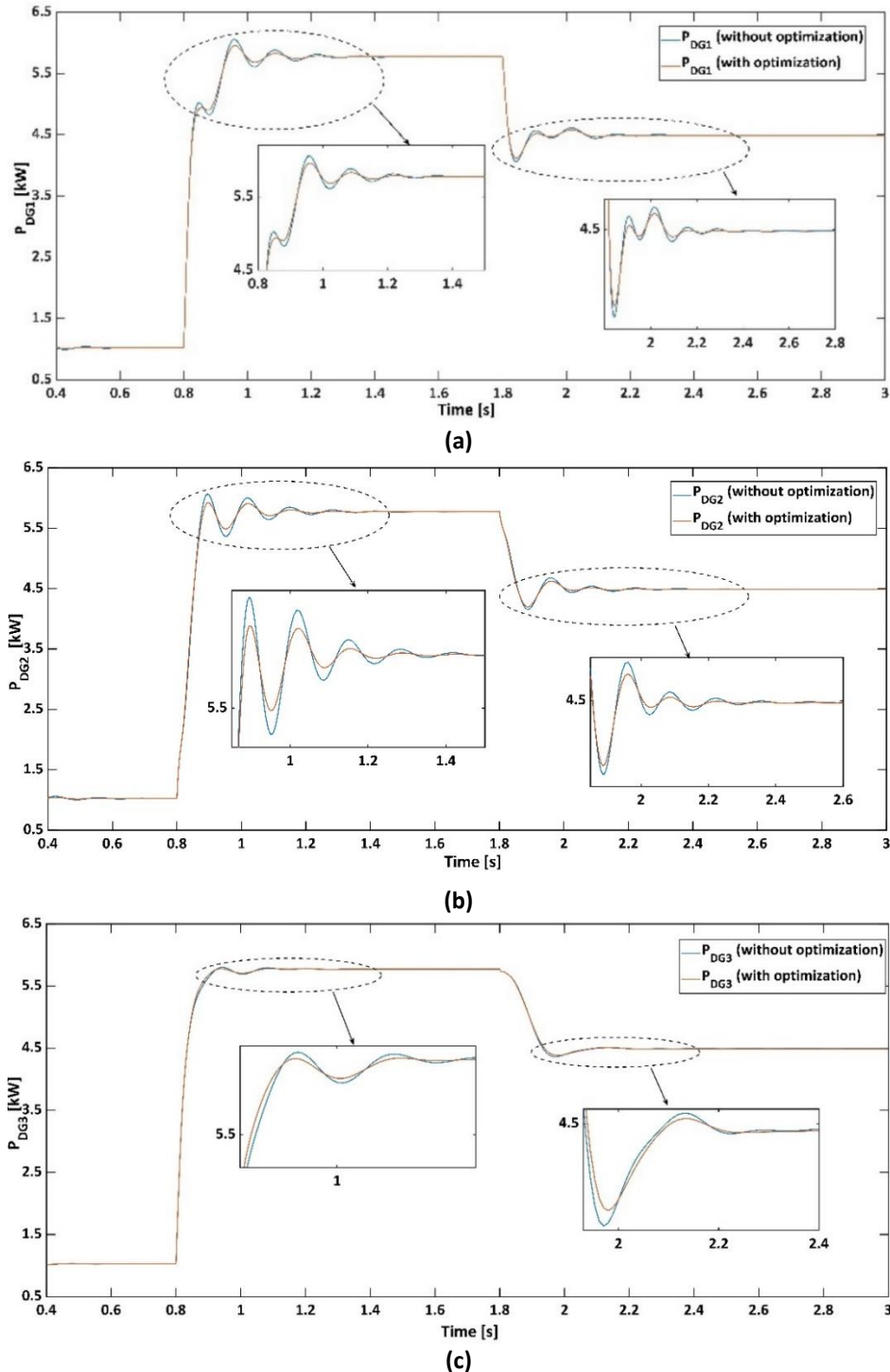

(a)

(b)

(c)

Fig. 10. DGs real power response in different modes with conventional and optimized droop controller parameters for *R* load: a) DG1; b) DG2; c) DG3.

The time to achieve a stable, steady response for the system is approximately 0.4 s with the proposed method, whereas it is more than 0.8 s with the conventional approach. Table 2 shows the comparison performance indices for DG real power response in different operating modes with conventional and optimized parameters.

Table 2. Comparison of performance indices of real power response for *R* load.

DGs real power	Without optimization		With optimization	
	Overshoot [%] (Islanded mode)	Undershoot [%] (Load cut-off mode)	Overshoot [%] (Islanded mode)	Undershoot [%] (Load cut-off mode)
P_{DG1}	4.85	9.53	3.2	8.33
P_{DG2}	5.08	7.39	2.55	6.48
P_{DG3}	0.13	2.87	0.05	2.4

As the load connected to the microgrid is only resistive, the reactive power amount is the drop in the inductive element of network lines. Even if the same reactive power droop gain is used, the reactive power shared by DGs is different because the reactive power distribution is dependent on the local bus voltage (node voltages) at the bus.

The reactive power sharing between different DGs is shown in Fig. 11. The transient oscillations are much reduced, and the steady state value is achieved much faster with the optimized controller.
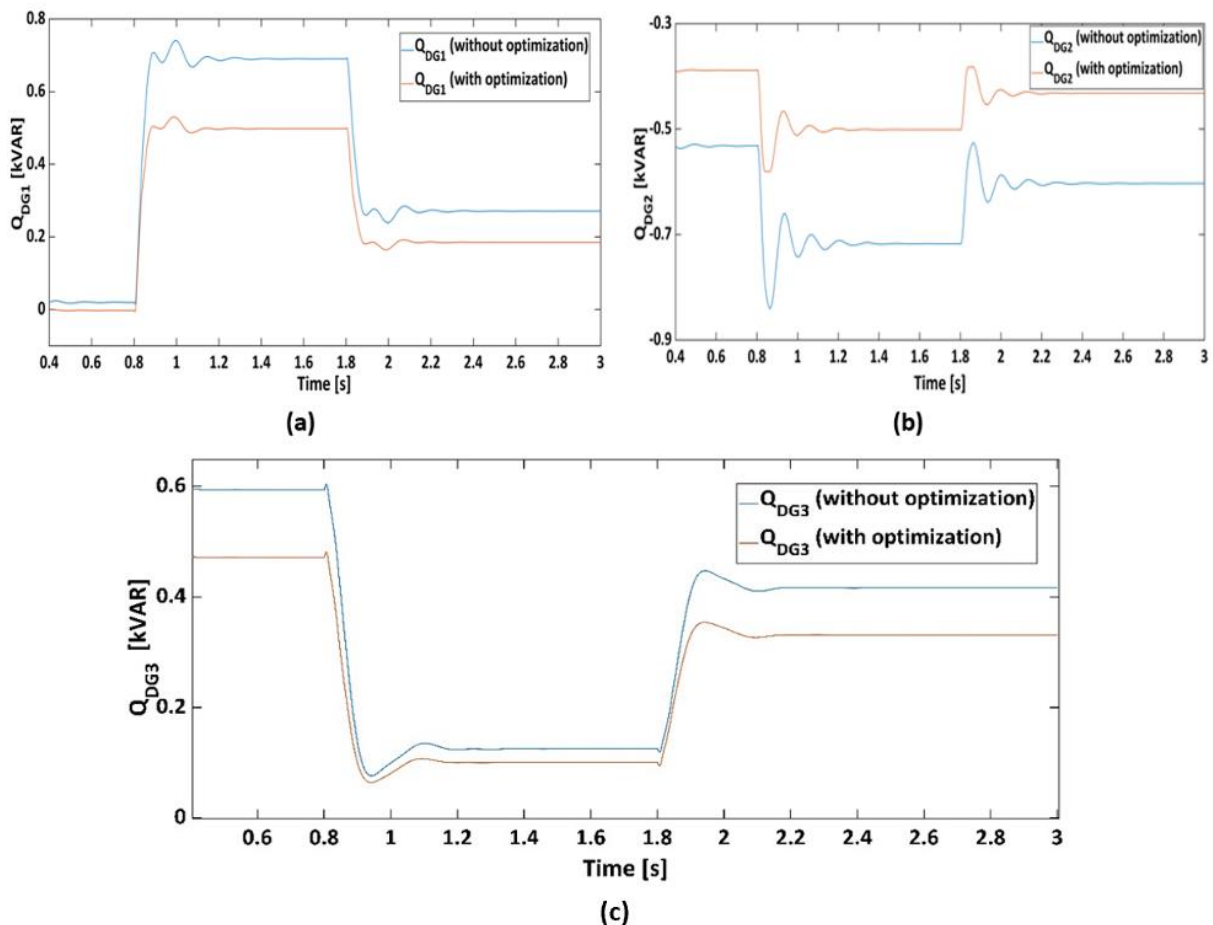

Fig. 11. DGs reactive power response in different modes with conventional and optimized droop controller parameters for *R* load: a) DG1; b) DG2; c) DG3.

The circulating currents i_{c1} (between DG1 and DG2) and i_{c2} (between DG2 and DG3) is shown in Fig. 12.

The results show that peak overshoot in i_{c1} is reduced by 0.6 A in islanded mode and 0.3 A in load cut-off mode, similarly for i_{c2} the peak overshoot is reduced by 0.5A and 0.2A in islanded and load cut-off mode correspondingly.

For both circulating currents, transient oscillations reduce drastically in magnitude. The circulating current almost becomes zero within 0.4 s with optimized parameters and within 0.6s conventional parameters.

The settling time is reduced by 0.2 s with optimized parameters. Fig. 13 and Fig. 14 show the variation in DGs' d-axis output voltages and d-axis output currents for different operating modes, respectively.
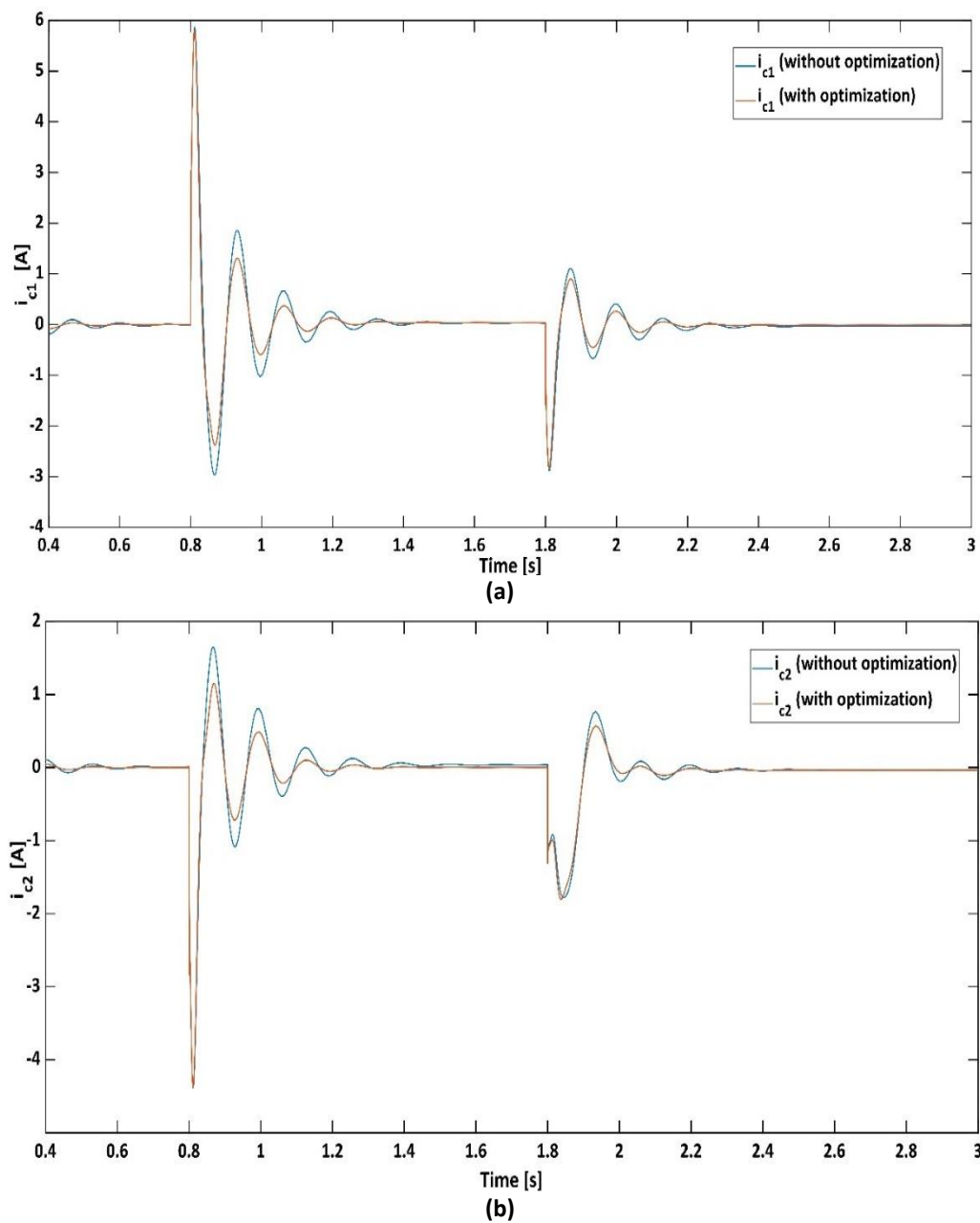

Fig. 12. Circulating current between DGs in different modes with conventional and optimized droop controller parameters for R load: a) i_{c1}; b) i_{c2}.
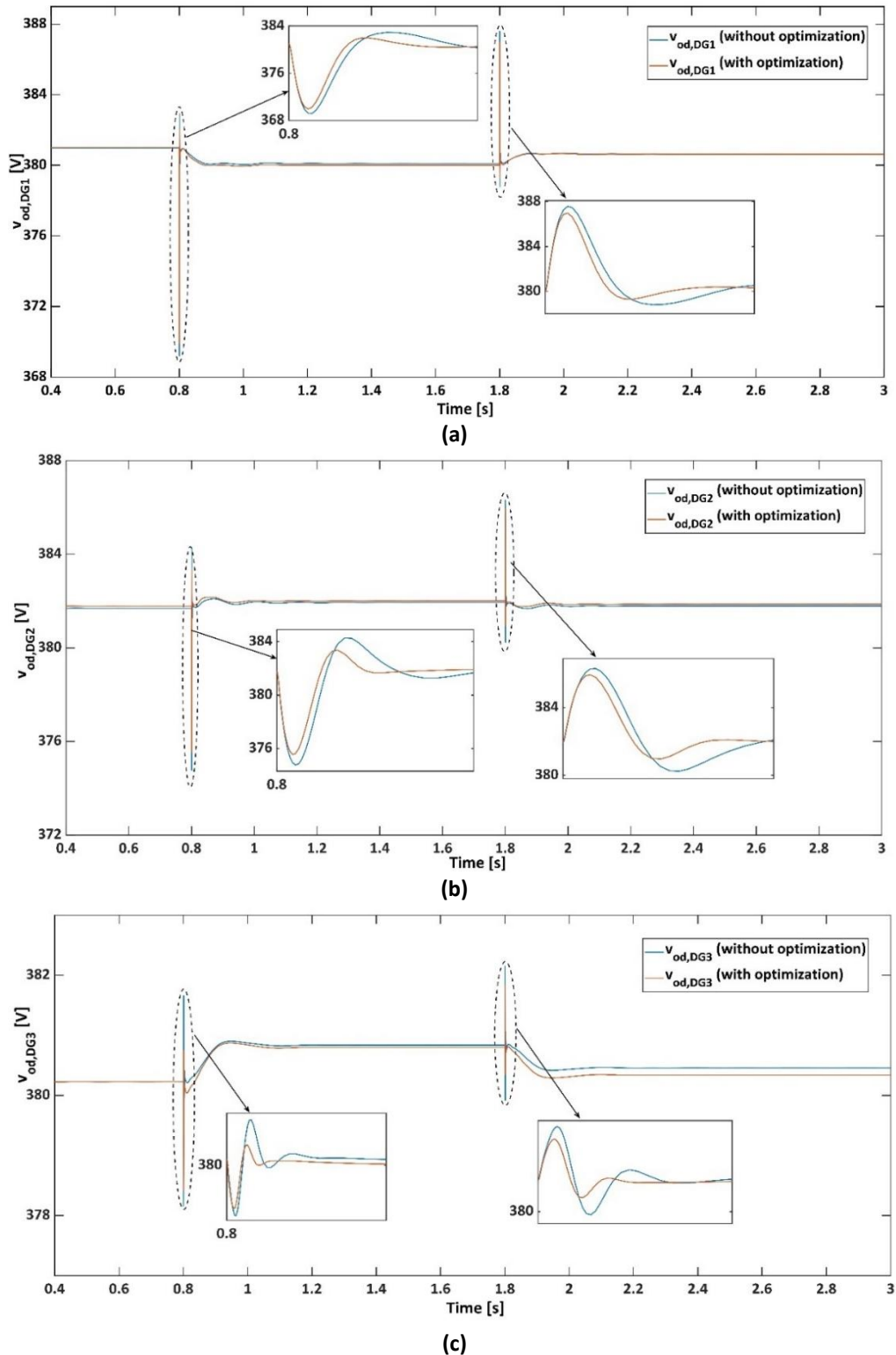
Fig. 13. DGs *d*-axis output voltage response in different modes with conventional and optimized droop controller parameters for *R* load: a) DG1; b) DG2; c) DG3.

From Fig. 13, it is observed that during switching operation, the overshot/undershoot is reduced by 0.2-0.3 % and settling time is reduced to 0.2 s in the case of optimized results as compared to conventional values for all output voltages. Fig. 14 indicates that the *d*-axis output current is highly oscillatory and takes much time to settle with conventional droop parameters. The transient magnitude of oscillations is reduced by 0.9%-4.3% in output current response and the steady state is achieved much faster.
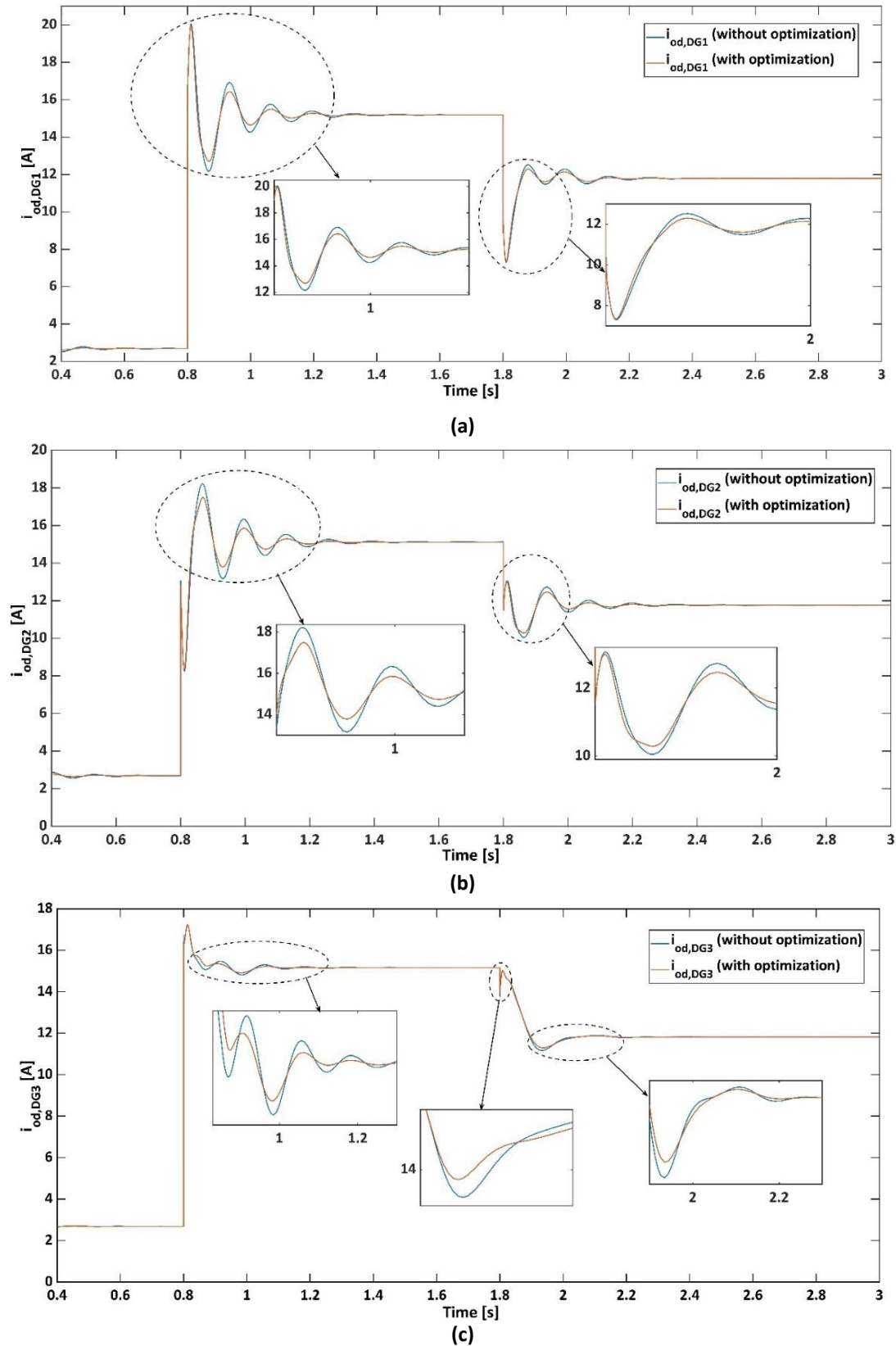
(a)

(b)

(c)

Fig. 14. DGs *d*-axis output current response in different modes with conventional and optimized droop controller parameters with *R* load: a) DG1; b) DG2; c) DG3.

The frequency response is much better with the proposed technique in all operating modes, as depicted in Fig. 15. The oscillations in frequency response decay quicker with the proposed approach than with the conventional droop controller.
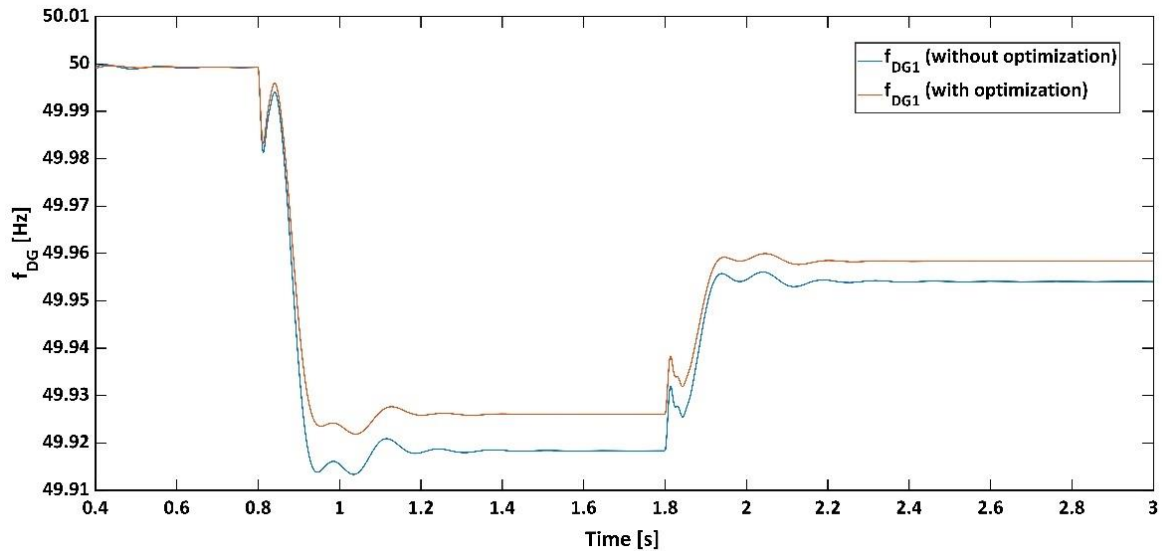
Fig. 15. DG1 frequency response with conventional and optimized droop controller parameters for *R* load.

Case 2: Considering Resistive-Inductive (*RL*) load.

In this case, the microgrid supplies power to the *RL* load. At t = 0.8 s, the grid is disconnected, and the microgrid operates in islanded mode, supplying the desired amount of active and reactive power to the load. At t = 0.8 s, the step reduction of load (8 kW and 3 kVAR) is applied, which is almost 50 % of the total load, to see the effect of droop parameters on the performance of the microgrid.

The time-domain simulation results for case 2 are discussed as follows:

Fig. 16 depicts the real power response of DGs for Different operating scenarios. The quantitative analysis is shown in Table 3. The overshoot in real power is decreased by 0.76%, 1.9%, and 3% for DG1, DG2, and DG3, respectively, for islanded mode. The decrease in undershoot is 1.1%, 0.9%, and 2.11% for DG1, DG2, and DG3, correspondingly in load cut-off mode. The real power is shared equally, and a steady state is achieved within 0.2 s with the proposed optimization approach.

Table 3. Comparison of performance indices of real power response for *RL* Load.

DGs real power	Without optimization		With optimization	
	Overshoot [%] (Islanded mode)	Undershoot [%] (Load cut-off mode)	Overshoot [%] (Islanded mode)	Undershoot [%] (Load cut-off mode)
P_{DG1}	5.83	2.6	5.07	1.5
P_{DG2}	10.23	6.35	8.33	5.46
P_{DG3}	60	29.88	57	27.11

The reactive power sharing with the proposed approach is presented in Fig. 17 for *RL* load. The reactive power supplied by DGs with optimized parameters is the same as conventional parameters. The transient response of reactive power is much better with the proposed approach than without optimization.

In the case of resistive load, the difference in reactive power sharing between the proposed and conventional approaches is large because the reactive power amount is less (in VARs). When the *RL* load is considered, the load also requires reactive power.

Fig. 16. DGs real power response in different modes with conventional and optimized droop controller parameters for *RL* load: a) DG1; b) DG2; c) DG3.

So, all the DGs must supply reactive power based on reactive power-voltage droop characteristics. Table 4 represents indices of reactive power-sharing among three DGs.
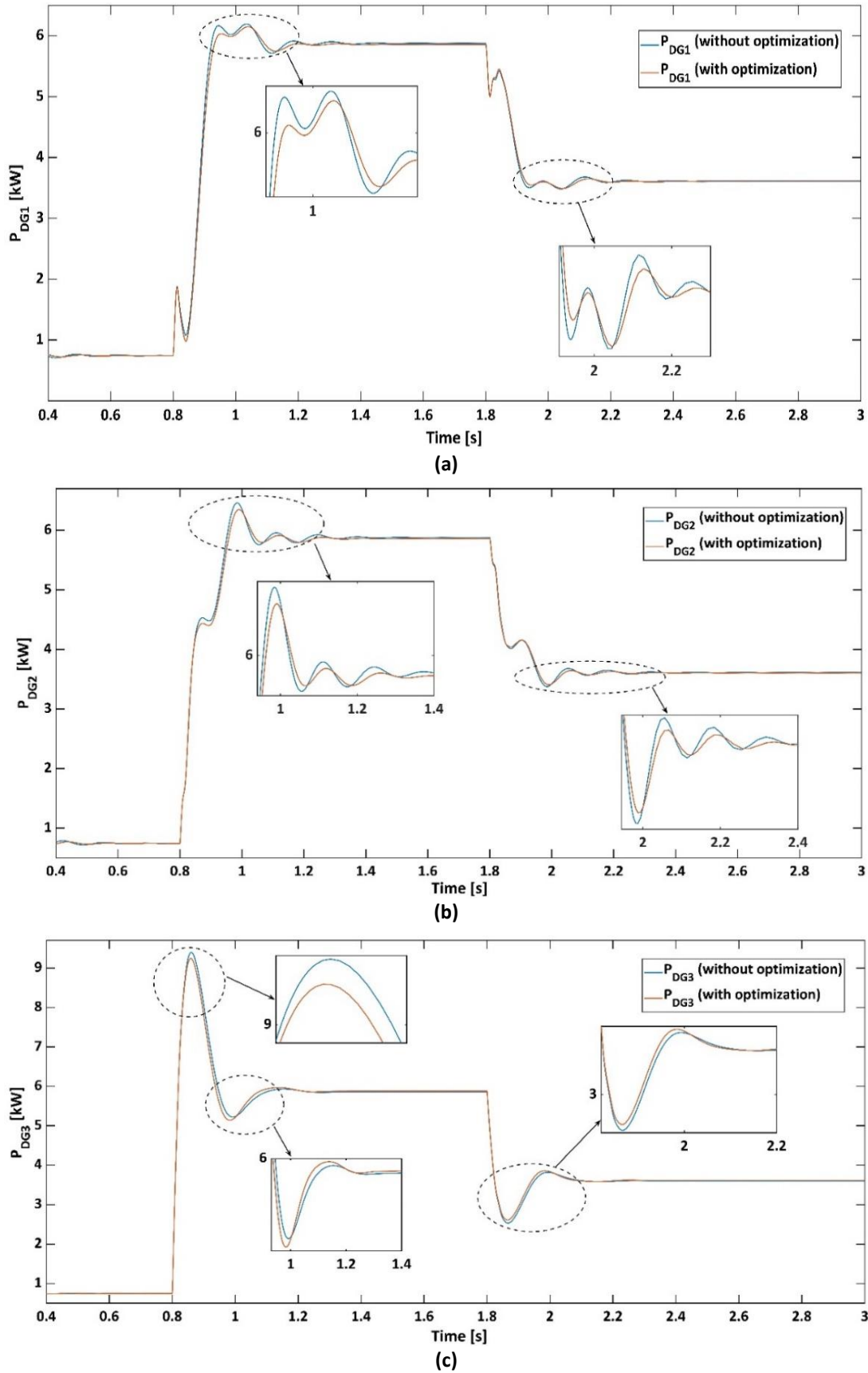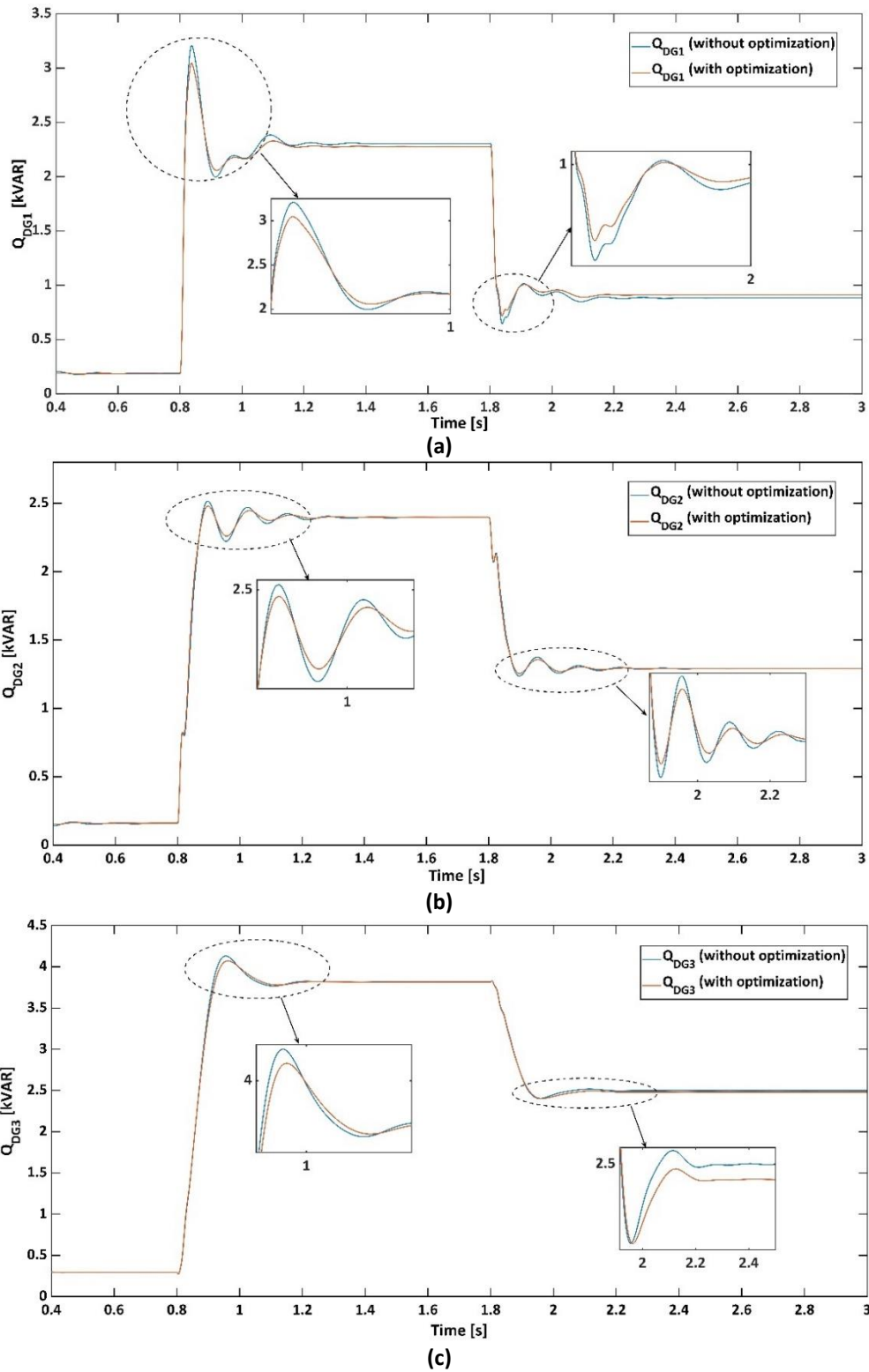
Fig. 17. DGs real power response in different modes with conventional and optimized droop controller parameters for *RL* load: a) DG1; b) DG2; c) DG3.

Table 4. Comparison of performance indices of reactive power response for *RL* Load.

DGs real power	Without optimization		With optimization	
	Overshoot [%] (Islanded mode)	Undershoot [%] (Load cut off mode)	Overshoot [%] (Islanded mode)	Undershoot [%] (Load cut-off mode)
Q_{DG1}	39	26.79	33.49	20.86
Q_{DG2}	4.83	4.19	3.38	2.64
Q_{DG3}	8.28	1.45	6.74	0.53

With the proposed approach, notable enhancements in the reactive power response. Specifically, overshoot is reduced by 5.6%, 1.45%, and 1.54% for DG1, DG2, and DG3, respectively, during islanded mode operation.

In load cut-off mode, the undershoot is reduced by 5.93%, 1.55%, and 0.92% for DG1, DG2, and DG3, respectively. Additionally, the settling time for reactive power is nearly 0.2 s, underscoring the proposed approach's effectiveness in improving the microgrid's dynamic behavior.

Fig. 18 represents the response of circulating current between DGs with *RL* load. The oscillations in both circulating currents are damped within 0.2 s, and the overshoot is reduced by 0.1 A.
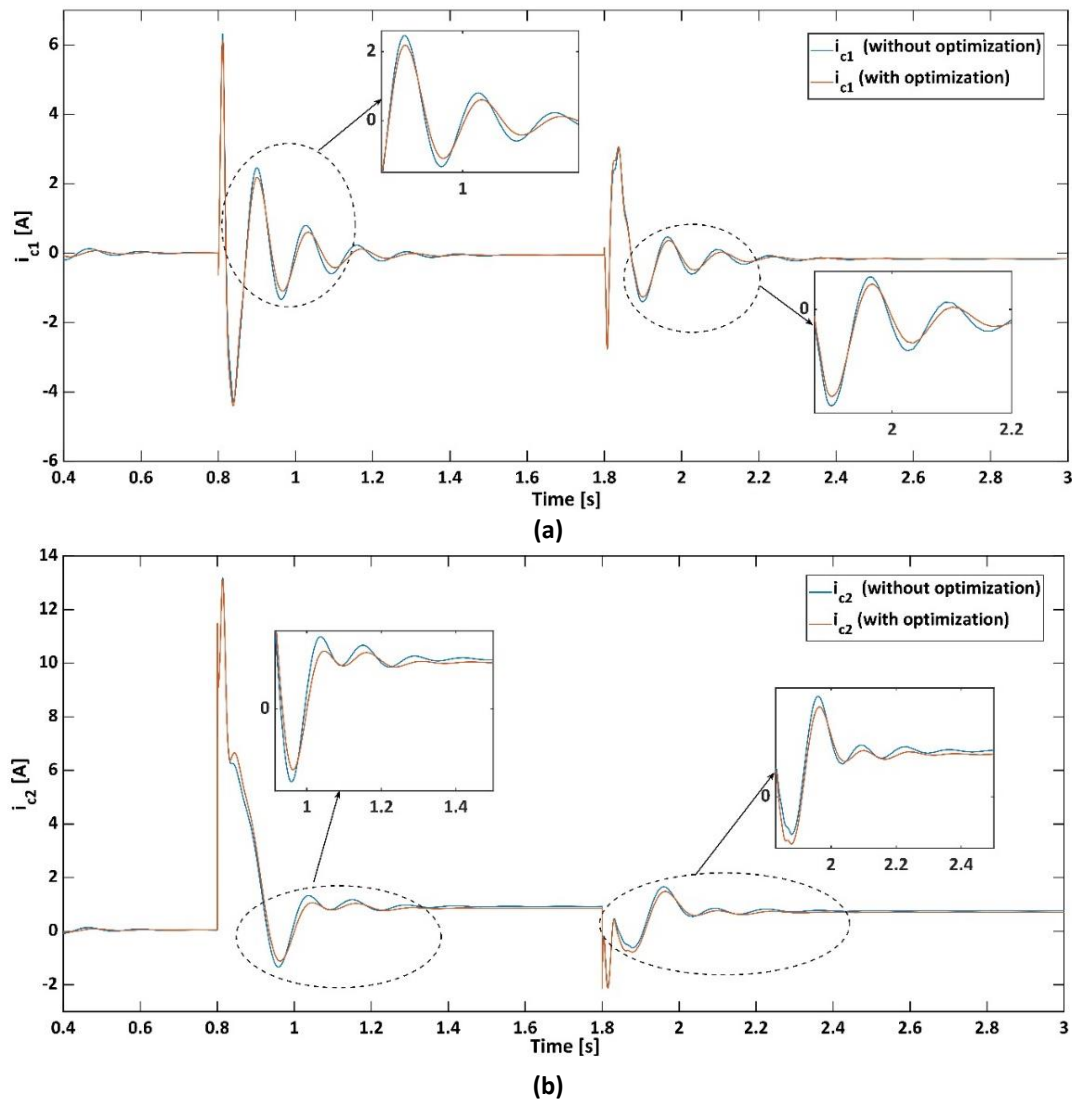

Fig. 18. Circulating current between DGs in different modes with conventional and optimized droop controller parameters for *RL* load: a) i_{c1}; b) i_{c2}.

Fig. 19 and Fig. 20 illustrate the behavior of *d*-axis output voltage and output current, respectively, under RL load conditions.

The oscillations in the output voltage waveforms are swiftly attenuated, achieving stability within 0.2 s, particularly when the microgrid's operating conditions undergo changes.

Across all the output voltage waveforms, there is a consistent reduction in both overshoot and undershoot, falling within the range of 0.5% to 2%.

Fig. 19. DGs *d*-axis output voltage response in different modes with conventional and optimized droop controller parameters for *RL* load: a) DG1; b) DG2; c) DG3.

The *d*-axis output current response exhibits pronounced high-frequency oscillations due to the significant RL load supplied by the DGs. However, by optimizing parameters, these oscillations are effectively mitigated, leading to a notable reduction in settling time, which now stands at just 0.2 s. Specifically, in islanded mode, there is a remarkable 5%, 3%, and 0.8% decrease in overshoot, and in load reduction mode, improvements in current response by

2.73%, 1.88%, and 3% are observed for DG1, DG2, and DG3, respectively with optimized parameters.
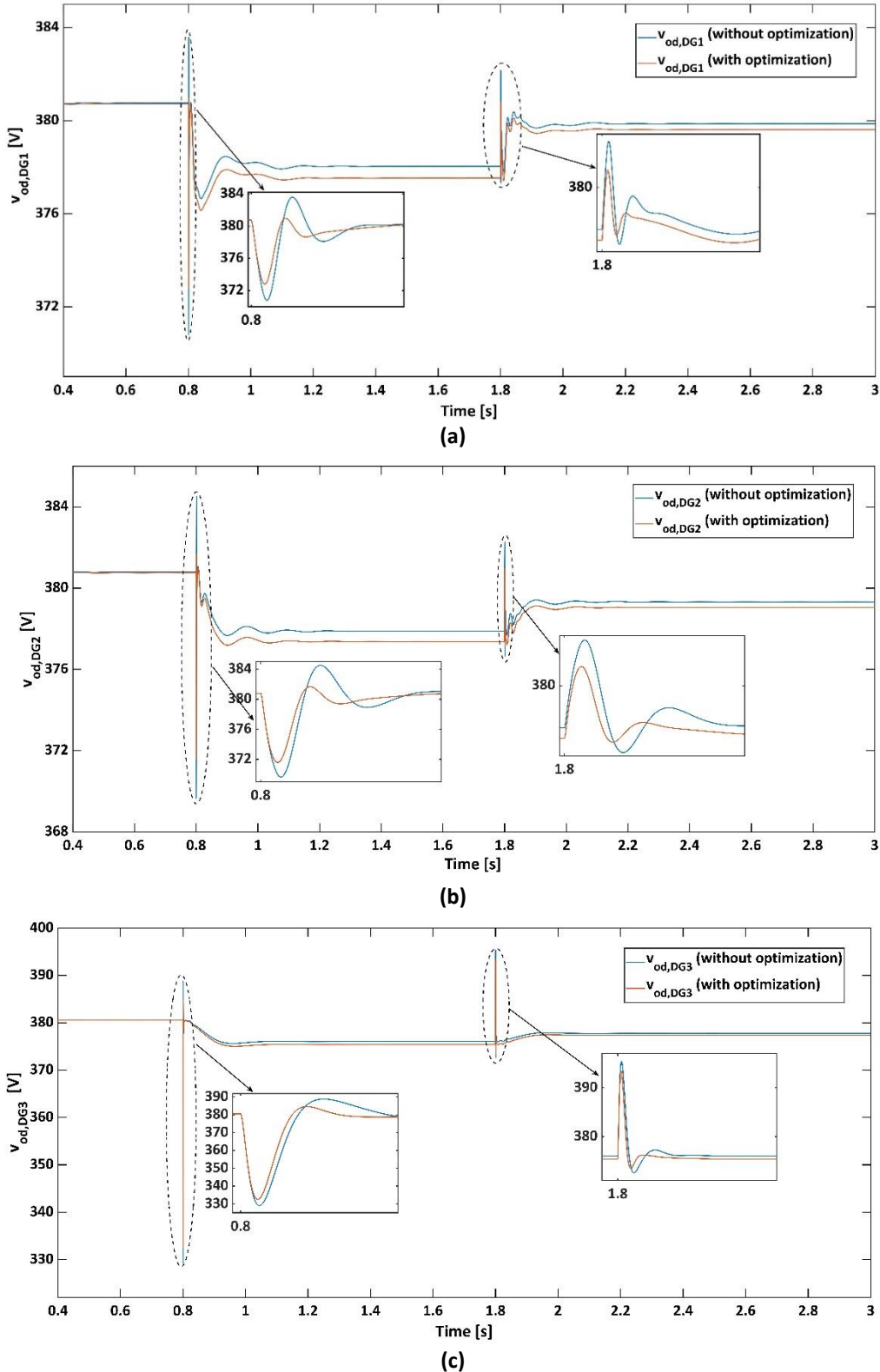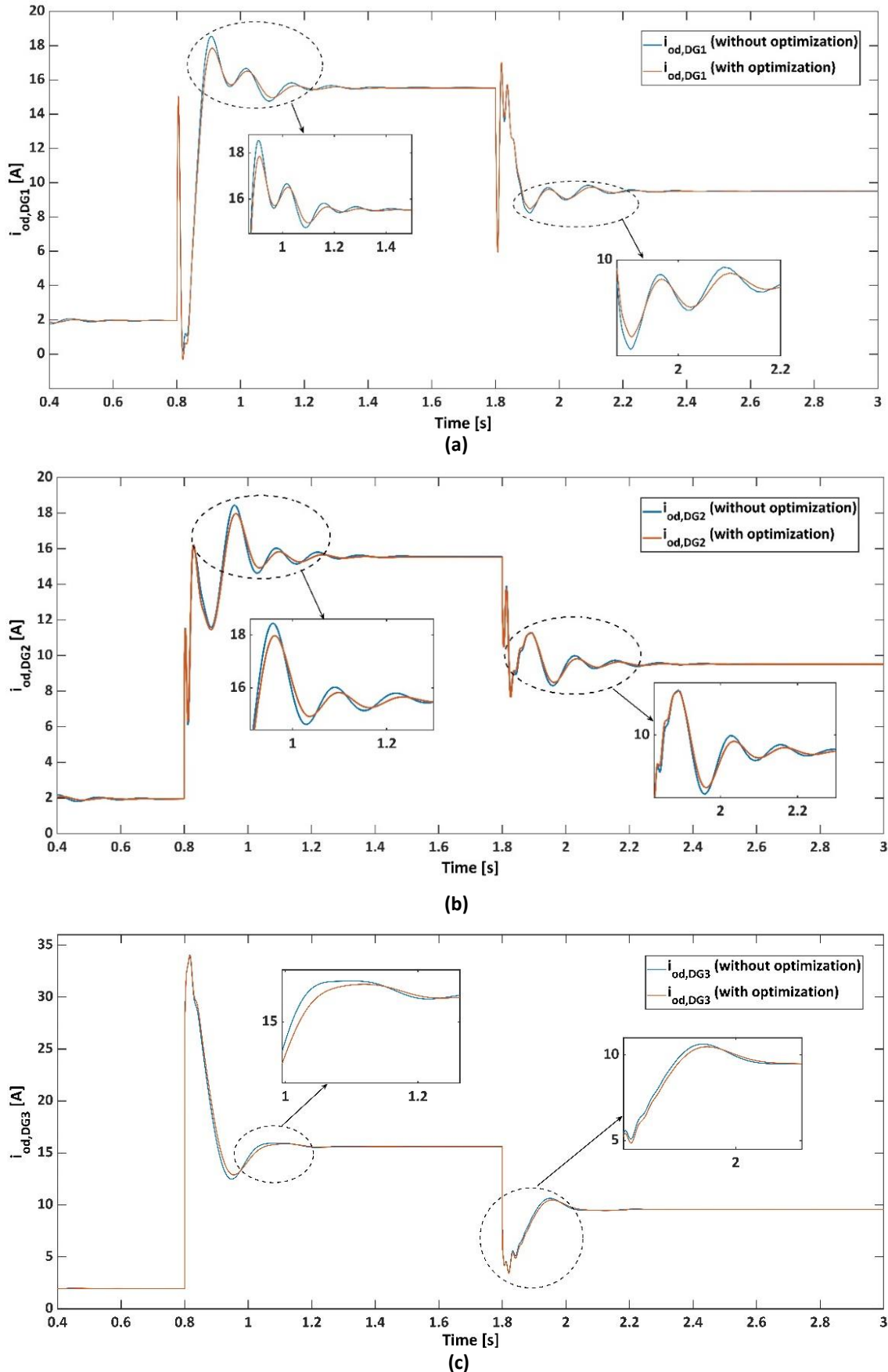

Fig. 20. DGs *d*-axis output current response in different modes with conventional and optimized droop controller parameters for *RL* load: a) DG1; b) DG2; c) DG3.

Fig. 21 presents the frequency response of DG1. With the proposed controller, it is evident that the frequency variation is effectively controlled and remains closely aligned with the nominal values, showcasing the controller's ability to maintain stable and reliable frequency levels.

The optimization parameters and their respective domains are obtained based on eigenvalue and sensitivity analyses. The outcomes of simulations provide compelling evidence that the proposed approach enhances the dampening of power oscillations and significantly accelerates the system's transition to a stable, steady state.
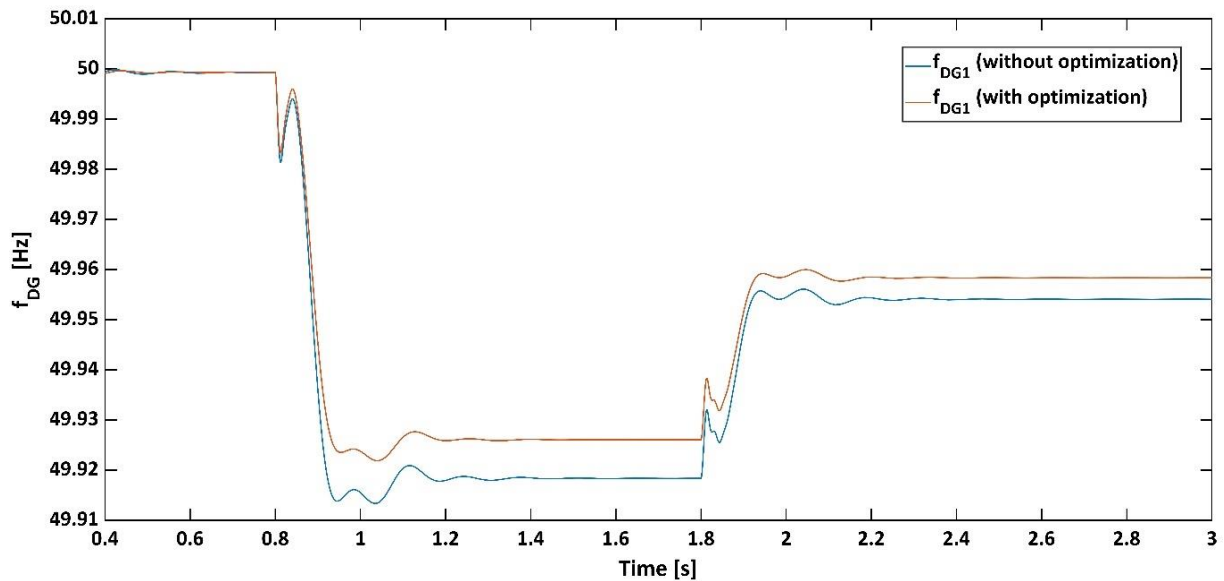

Fig. 21. DG1 frequency response with conventional and optimized droop controller parameters for *RL* load.

6. CONCLUSIONS

The detailed and acute state-space model of a microgrid incorporating various elements such as interfacing inverter control, coupling filter, distribution line, and load dynamics all synchronized through a common reference frame, is developed in this paper.

The eigenvalue analysis and sensitivity analysis are performed to demonstrate that low-frequency dominant modes are notably affected by power controller parameters and depend on droop gains m_p and n_q. The integral time-squared error of DG output powers is selected as an optimization objective function to find the optimal parameter value. Simulation results and eigenvalue plot in MATLAB /Simulink validate that the droop parameters have inmost effects on stability and dynamic performance under mode change.

The parameters obtained from the proposed control optimization scheme considerably contribute to preserving the microgrid stability by dampening the oscillations and establishing a steady state more quickly, as observed from time domain simulations.

The simulation results for two different load conditions show that improvement in real power response ranges from 0.5% to 3%, and settling time is reduced to 0.2 s. Hence, the proposed approach serves as a valuable contribution to preserving microgrid stability and the parameter selection of the droop controller.

APPENDIX: THE DETAILED MODELLING EQUATIONS

In Eq. (11),

$$
A_{dgi} = \begin{bmatrix}
0 & -m_p & 0 & 0 & 0 & 0 & 0 & 0 & 0 & 0 & 0 & 0 & 0 \\
0 & -\omega_c & 0 & 0 & 0 & 0 & 0 & 0 & 0 & \omega_c I_{od} & \omega_c I_{oq} & \omega_c V_{od} & \omega_c V_{oq} \\
0 & 0 & -\omega_c & 0 & 0 & 0 & 0 & 0 & 0 & -\omega_c I_{oq} & \omega_c I_{od} & \omega_c V_{oq} & -\omega_c v_{od} \\
0 & 0 & -n_q & 0 & 0 & 0 & 0 & 0 & 0 & -1 & 0 & 0 & 0 \\
0 & 0 & 0 & 0 & 0 & 0 & 0 & 0 & 0 & 0 & -1 & 0 & 0 \\
0 & 0 & -n_q k_{pv} & k_{iv} & & & -1 & & & -k_{pv} & -\omega_n C_f & G_f & 0 \\
0 & 0 & 0 & 0 & k_{iv} & & & 0 & -1 & \omega_n C_f & -k_{pv} & 0 & G_f \\
0 & -m_p I_{lq} & \dfrac{-n_q k_{pv} k_{pc}}{L_f} & \dfrac{k_{iv} k_{pc}}{L_f} & 0 & \dfrac{k_{ic}}{L_f} & \dfrac{-k_{pc}-R_f}{L_f} & \omega_0-\omega_n & \dfrac{-k_{pv}k_{pc}-1}{L_f} & -\dfrac{\omega_n C_f k_{pc}}{L_f} & \dfrac{k_{pc}G_f}{L_f} & 0 \\
0 & m_p I_{ld} & 0 & & \dfrac{k_{iv}k_{pc}}{L_f} & 0 & \dfrac{k_{ic}}{L_f} & \omega_n-\omega_0 & \dfrac{-k_{pc}-R_f}{L_f} & \dfrac{\omega_n C_f k_{pc}}{L_f} & \dfrac{-k_{pv}k_{pc}-1}{L_f} & & \dfrac{k_{pc}G_f}{L_f} \\
0 & -m_p V_{oq} & 0 & & & \dfrac{1}{C_f} & 0 & 0 & \omega_0 & -\dfrac{1}{C_f} & 0 \\
0 & m_p V_{od} & 0 & & & \dfrac{1}{C_f} & -\omega_0 & 0 & 0 & -\dfrac{1}{C_f} \\
\dfrac{V_{bD}\sin\delta_0 - V_{bQ}\cos\delta_0}{L_c} & -m_p I_{oq} & 0 & & & & \dfrac{1}{L_c} & 0 & -\dfrac{r_c}{L_c} & \omega_0 \\
\dfrac{V_{bD}\cos\delta_0 + V_{bQ}\sin\delta_0}{L_c} & m_p I_{od} & 0 & & & & \dfrac{1}{L_c} & -\omega_0 & -\dfrac{r_c}{L_c}
\end{bmatrix}
\tag{A.1}
$$

where subscript 0 indicates initial value of all variables

$$
B_{i\omega com} = \begin{bmatrix} -1 & 0 & \ldots & 0 \end{bmatrix}^T_{1\times13}, \quad
B_{dgi} = \begin{bmatrix}
0 & \ldots & 0 & -\dfrac{\cos\delta_0}{L_c} & -\dfrac{\sin\delta_0}{L_c} \\
0 & \ldots & 0 & \dfrac{\sin\delta_0}{L_c} & -\dfrac{\cos\delta_0}{L_c}
\end{bmatrix}
\tag{A.2}
$$

In Eq. (12),

$$
C_{dg\omega i} = \begin{cases}
\begin{bmatrix} 0 & -m_p & \ldots & 0 \end{bmatrix}_{1\times13}, & i=1; \\
\begin{bmatrix} 0 & \ldots & 0 \end{bmatrix}_{1\times13}, & i\neq1
\end{cases}
$$

$$
C_{dgci} = \begin{bmatrix}
-I_{od}\sin\delta_0 - I_{oq}\cos\delta_0 & 0 & \ldots & 0 & \cos\delta_0 & -\sin\delta_0 \\
I_{od}\cos\delta_0 - I_{oq}\sin\delta_0 & 0 & \ldots & 0 & \sin\delta_0 & \cos\delta_0
\end{bmatrix}
\tag{A.3}
$$

In Eq. (14),

$$
A_{DG} = \begin{bmatrix}
A_{dg1} + B_{1\omega com}C_{dg\omega1} & 0 & 0 & . \\
0 & A_{dg2} + B_{2\omega com}C_{dg\omega1} & 0 & . \\
. & . & . & . \\
. & . & . & A_{dgs} + B_{s\omega com}C_{dg\omega1}
\end{bmatrix}_{13s\times13s}
\tag{A.4}
$$

$$
B_{DG} = \begin{bmatrix}
B_{dg1} \\
B_{dg2} \\
. \\
. \\
B_{dgs}
\end{bmatrix}_{13s\times2m}
\quad \& \quad
\begin{bmatrix} \Delta v_{bDQ} \end{bmatrix} = \begin{bmatrix} \Delta v_{bDQ1} & \Delta v_{bDQ2} & . & . & \Delta v_{bDQm} \end{bmatrix}
\tag{A.5}
$$

In Eq. (15),

$$
C_{DGC} = \begin{bmatrix} \begin{bmatrix} C_{dgc1} \end{bmatrix} & 0 & 0 & . \\ 0 & \begin{bmatrix} C_{dgc2} \end{bmatrix} & 0 & . \\ . & . & . & . \\ . & . & . & \begin{bmatrix} C_{dgcs} \end{bmatrix} \end{bmatrix}_{2s \times 13s} \tag{A.6}
$$

In Eq. (18),

$$
A_{linei} = \begin{bmatrix} \dfrac{-r_{linei}}{L_{linei}} & \omega_0 \\ -\omega_0 & \dfrac{-r_{linei}}{L_{linei}} \end{bmatrix} \quad \& \quad A_{LINE} = \begin{bmatrix} A_{line1} & 0 & \ldots & 0 \\ 0 & A_{line2} & \ldots & 0 \\ 0 & 0 & \ldots & 0 \\ 0 & 0 & \ldots & A_{linen} \end{bmatrix}_{2n \times 2n} \tag{A.7}
$$

$$
B_{1linei} = \begin{bmatrix} \dfrac{1}{L_{linei}} & 0 & -\dfrac{1}{L_{linei}} & 0 & 0 & 0 \\ 0 & \dfrac{1}{L_{linei}} & 0 & -\dfrac{1}{L_{linei}} & 0 & 0 \end{bmatrix}_{2 \times 2m} \quad \& \quad B_{1LINE} = \begin{bmatrix} B_{1line1} \\ B_{1line2} \\ \ldots \\ \ldots \\ B_{1linen} \end{bmatrix}_{2n \times (2m)} \tag{A.8}
$$

$$
B_{2linei} = \begin{bmatrix} I_{lineQi} \\ -I_{lineDi} \end{bmatrix} \quad \& \quad B_{2LINE} = \begin{bmatrix} B_{2line1} \\ B_{2line2} \\ \ldots \\ \ldots \\ B_{2linen} \end{bmatrix}_{2n \times 1} \tag{A.9}
$$

In Eq. (24),

$$
A_{loadi} = \begin{bmatrix} \dfrac{-R_{loadi}}{L_{loadi}} & \omega_0 \\ -\omega_0 & \dfrac{-R_{loadi}}{L_{loadi}} \end{bmatrix} \quad \& \quad A_{LOAD} = \begin{bmatrix} A_{load1} & 0 & \ldots & 0 \\ 0 & A_{load2} & \ldots & 0 \\ 0 & 0 & \ldots & 0 \\ 0 & 0 & \ldots & A_{loadp} \end{bmatrix}_{2p \times 2p} \tag{A.10}
$$

$$
B_{1loadi} = \begin{bmatrix} \ldots & \dfrac{1}{L_{loadi}} & 0 & \ldots \\ \ldots & 0 & \dfrac{1}{L_{loadi}} & \ldots \end{bmatrix} 2 \times (2m) \quad \& \quad B_{1LOAD} = \begin{bmatrix} B_{1load1} \\ B_{1load2} \\ \ldots \\ \ldots \\ B_{1loadp} \end{bmatrix}_{2p \times (2m)} \tag{A.11}
$$

$$
B_{2loadi} = \begin{bmatrix} I_{loadQi} \\ -I_{loadDi} \end{bmatrix} \quad \& \quad B_{2LOAD} = \begin{bmatrix} B_{2load1} \\ B_{2load2} \\ \ldots \\ \ldots \\ B_{2loadp} \end{bmatrix}_{2p \times 1} \tag{A.12}
$$

In Eq. (29),

$$A_{mg} = \begin{bmatrix} A_{DG} + B_{DG}R_{VN}M_{DG}C_{DGc} & B_{DG}R_{VN}M_{LINE} & B_{DG}R_{VN}M_{LOAD} \\ B_{1LINE}R_{VN}M_{DG}C_{DGc} + B_{2LINE}C_{DG\omega} & A_{LINE} + B_{1LINE}R_{VN}M_{LINE} & B_{1LINE}R_{VN}M_{LOAD} \\ B_{1LOAD}R_{VN}M_{DG}C_{DGc} + B_{2LOAD}C_{DG\omega} & B_{1LOAD}R_{VN}M_{LINE} & A_{LOAD} + B_{1LOAD}R_{VN}M_{LOAD} \end{bmatrix} \quad (A.13)$$

Table A-1. DG controller parameters.

Parameter	Value	Parameter	Value
f_s	8 kHz	m_p	9.4×10^{-5}
L_f	1.35 mH	n_q	1.3×10^{-3}
C_f	50 μF	k_{pv}	0..05
r_f	0.1 Ω	k_{iv}	390
L_c	0.35 mH	k_{pc}	10.5
r_{Lc}	0.03 Ω	k_{ic}	16×10^3
ω_{cf}	31.41 rad/s	G_f	0.75

REFERENCES

[1] A. Arfoa, E. Almaita, S. Alshkoor, M. Shloul, "Techno-economic feasibility analysis of on-grid battery energy storage system: Almanara PV power plant case study," *Jordan Journal of Electrical Engineering*, vol. 8, no. 3, p. 254, 2022, doi: 10.5455/jjee.204-1654330119.

[2] E. Jamshidpour, S. Saadate, P. Poure, "Energy management and control of a stand-alone photovoltaic/ultracapacitor/battery microgrid," Jordan Conference on Applied Electrical Engineering and Computing Technologies, 2015, doi: 10.1109/AEECT.2015.7360584.

[3] A. Gavilema, J. Gil, J. Hervás, J. Moreno, M. García, "Modeling and energy management of a microgrid based on predictive control strategies," *Solar*, vol. 3, no. 1, pp. 62-73, doi: 10.3390/solar3010005.

[4] S. Chandak, P. Rout, "The implementation framework of a microgrid: a review," *International Journal of Energy Research*, vol. 45, no. 3, pp. 3523-3547, 2021, doi: 10.1002/er.6064.

[5] M. Legha, S. Rashidifard, "Energy management in multiple micro-grids considering uncertainties of load using hierarchical multi-agent system," *Journal of Electrical Engineering*, vol. 7, no. 2, 2021, doi: 10.5455/jjee.204-1612950717.

[6] J. Wang, G. Saraswat, "Study of Inverter Control Strategies on the Stability of Low-Inertia Microgrid Systems," Annual Conference of the IEEE Industrial Electronics Society, 2022, doi: 10.1109/IECON49645.2022.9968525.

[7] M. Abbasi, E. Abbasi, L. Li, R. Aguilera, D. Lu, F. Wang, "Review on the Microgrid Concept, Structures, Components, Communication Systems, and Control Methods," *Energies*, vol. 16, no. 1, p. 484, 2023, doi: 10.3390/en16010484.

[8] G. Shahgholian, "A brief overview of microgrid performance improvements using distributed FACTS devices," *Journal of Renewable Energy and Environment* vol. 10, no. 1, pp. 43-58, 2023, doi: 10.30501/jree.2022.321435.1305.

[9] F. Mohammadi, H. Vanashi, A. Feliachi, "State-space modeling, analysis, and distributed secondary frequency control of isolated microgrids," *IEEE Transactions on Energy Conversion*, vol. 33, no. 1, pp. 155-165, 2017, doi: 10.1109/TEC.2017.2757012.

[10] H. Cheng, Z. Shuai, C. Shen, X. Liu, Z. Li, and Z. Shen, "Transient angle stability of paralleled synchronous and virtual synchronous generators in islanded microgrids," *IEEE Transactions on Power Electronics*, vol. 35, no. 8, pp. 8751-8765, 2020, doi: 10.1109/TPEL.2020.2965152.

[11] M. Azab, "High performance decoupled active and reactive power control for three-phase grid-tied inverters using model predictive control," *Protection and Control of Modern Power Systems,* vol. 6, no. 1, p. 25, doi: 10.1186/s41601-021-00204-z.

[12] H. Sellamna, A. Pavan, A. Mellit, J. Guerrero, "An iterative adaptive virtual impedance loop for reactive power sharing in islanded meshed microgrids," *Sustainable Energy, Grids and Networks,* vol. 24, p. 100395, 2020, doi: 10.1016/j.segan.2020.100395.

[13] A. Hirsch, Y. Parag, J. Guerrero, "Microgrids: A review of technologies, key drivers, and outstanding issues," *Renewable and Sustainable Energy Reviews,* vol. 90, pp. 402-411, 2018, doi: 10.1016/j.rser.2018.03.040.

[14] X. Chen, C. Zhang, Q. Huang, M. Oduro, "Small-signal modeling and analysis of grid-connected Inverter with power differential droop control," *Mathematical Problems in Engineering,* vol. 2016, p. 3965945, 2016, doi: 10.1155/2016/3965945.

[15] N. Pogaku, M. Prodanovic, T. Green, "Modeling, analysis and testing of autonomous operation of an inverter-based microgrid," *IEEE Transactions on Power Electronics,* vol. 22, no. 2, pp. 613-625, 2007, doi: 10.1109/TPEL.2006.890003.

[16] P. Raju, T. Jain, "Small signal modelling and stability analysis of an islanded AC microgrid with inverter interfaced DGs," International Conference on Smart Electric Grid, 2014, doi: 10.1109/ISEG.2014.7005388.

[17] S. Ogbikaya, M. Iqbal, "Reduced order model of a microgrid system for a university community in Nigeria," *Jordan Journal of Electrical Engineering,* vol. 8, no. 3, pp. 266-278, 2022, doi: 10.5455/jjee.204-1653940509.

[18] M. Rasheduzzaman, J. Mueller, J. Kimball, "Reduced-order small-signal model of microgrid systems," *EEE Transactions on Sustainable Energy,* vol. 6, no. 4, pp. 1292-1305, 2015, doi: 10.1109/TSTE.2015.2433177.

[19] J. Chen, J. Chen, "Stability analysis and parameters optimization of islanded microgrid with both ideal and dynamic constant power loads," *IEEE Transactions on Industrial Electronics,* vol. 65, no. 4, pp. 3263-3274, 2017, doi: 10.1109/TIE.2017.2756588.

[20] X. Wang, H. Qing, P. Huang, C. Zhang, "Modeling and stability analysis of parallel inverters in island microgrid," *Electronics,* vol. 9, no. 3, p. 463, 2020, doi: 10.3390/electronics9030463.

[21] F. Katiraei, M. Iravani, P. Lehn, "Small-signal dynamic model of a micro-grid including conventional and electronically interfaced distributed resources," *IET Generation, Transmission & Distribution,* vol. 1, no. 3, pp. 369-378, 2007, doi: 10.1049/iet-gtd:20045207.

[22] M. Hassan, M. Abido, "Optimal design of microgrids in autonomous and grid-connected modes using particle swarm optimization," *IEEE Transactions on Power Electronics,* vol. 26, no. 3, pp. 755-769, 2010, doi: 10.1109/TPEL.2010.2100101.

[23] K. Yu, Q. Ai, S. Wang, J. Ni, T. Lv, "Analysis and optimization of droop controller for microgrid system based on small-signal dynamic model," *IEEE Transactions on Smart Grid,* vol. 7, no. 2, pp. 695-705, 2015, doi: 10.1109/TSG.2015.2501316.

[24] S. Eberlein, K. Rudion, E. Systems, "Small-signal stability modelling, sensitivity analysis and optimization of droop controlled inverters in LV microgrids," *International Journal of Electrical Power & Energy Systems,* vol. 125, p. 106404, 2021, doi: 10.1016/j.ijepes.2020.106404.

[25] M. Khan, E. Ahmed, S. Habib, Z. Ali, "Multi-objective optimization technique for droop controlled distributed generators in AC islanded microgrid," *Electric Power Systems Research,* vol. 213, p. 108671, 2022, doi: 10.1016/j.epsr.2022.108671.

[26] Y. Chen, J. Zhao, K. Qu, F. Li, "A PQ control strategy for voltage-controlled inverters applied in low-voltage power system," International Power Electronics and Application Conference and Exposition, 2014, doi: 10.1109/PEAC.2014.7037968.

[27] X. Meng, J. Liu, Z. Liu, "A generalized droop control for grid-supporting inverter based on comparison between traditional droop control and virtual synchronous generator

control," *IEEE Transactions on Power Electronics,* vol. 34, no. 6, pp. 5416-5438, 2018, doi: 10.1109/TPEL.2018.2868722.

[28] M. Ramezani, S. Li, Y. Sun, "Combining droop and direct current vector control for control of parallel inverters in microgrid," *IET Renewable Power Generation,* vol. 11, no. 1, pp. 107-114, 2017, doi: 10.1049/iet-rpg.2016.0107.

[29] A. Egwebe, M. Fazeli, P. Igic, P. Holland, "Implementation and stability study of dynamic droop in islanded microgrids," *IEEE Transactions on energy conversion,* vol. 31, no. 3, pp. 821-832, 2016, doi: 10.1109/TEC.2016.2540922.

[30] M. Jain, V. Saihjpal, N. Singh, S. Singh, "An overview of variants and advancements of PSO algorithm," *Applied Sciences,* vol. 12, no. 17, p. 8392, 2022, doi: 10.3390/app12178392.

[31] C. Rohit, P. Darji, H. Jariwala, "Modelling and control of static synchronous series compensator interfaced with DFIG-based wind farm using PSO for SSR alleviation," *International Journal of Ambient Energy,* vol. 43, no. 1, pp. 6449-6462, 2022, doi: 10.1080/01430750.2021.2023630.

[32] M. Leu, M. Yeh, "Grey particle swarm optimization," *Applied Soft Computing* vol. 12, no. 9, pp. 2985-2996, 2012, doi: 10.1016/j.asoc.2012.04.030.

[33] K. Chen, F. Zhou, L. Yin, S. Wang, Y. Wang, F. Wan, "A hybrid particle swarm optimizer with sine cosine acceleration coefficients," *Information Sciences,* vol. 422, pp. 218-241, 2018, doi: 10.1016/j.ins.2017.09.015.

[34] N. Zeng, Z. Wang, W. Liu, H. Zhang, K. Hone, X. Liu, "A dynamic neighborhood-based switching particle swarm optimization algorithm," *IEEE Transactions on Cybernetics* vol. 52, no. 9, pp. 9290-9301, 2020, doi: 10.1109/TCYB.2020.3029748.

[35] L. Xu, B. Song, M. Cao, "An improved particle swarm optimization algorithm with adaptive weighted delay velocity," *Systems Science Control Engineering,* vol. 9, no. 1, pp. 188-197, 2021, doi: 10.1080/21642583.2021.1891153.